THESIS

DIABATIC AND FRICTIONAL FORCING EFFECTS ON THE STRUCTURE AND

INTENSITY OF TROPICAL CYCLONES

Submitted by

Christopher J. Slocum

Department of Atmospheric Science

In partial fulfillment of the requirements

For the Degree of Master of Science

Colorado State University

Fort Collins, Colorado

Fall 2013

Master's Committee:

    Advisor: Wayne H. Schubert
    Co-Advisor: Mark DeMaria

    Russ S. Schumacher
    Michael J. Kirby
    Michael Fiorino

ABSTRACT

DIABATIC AND FRICTIONAL FORCING EFFECTS ON THE STRUCTURE AND

INTENSITY OF TROPICAL CYCLONES

Tropical cyclone intensity forecasting skill has slowed in improvement for both dynamical and statistical-dynamical forecasting methods in comparison to gains seen in track forecasting skill. Also, forecast skill related to rapid intensification, e.g. a 30 kt or greater increase in intensity within a 24-hour period, still remains poor. In order to make advances and gain a greater understanding, the processes that affect intensity change, especially rapid intensification, need further study. This work evaluates the roles of diabatic and frictional forcing on the structure and intensity of tropical cyclones.

To assess the diabatic forcing effects on intensity change in tropical cyclones, this study develops applications of Eliassen's balanced vortex model to obtain one-dimensional solutions to the geopotential tendency and two-dimensional solutions to the transverse circulation. The one-dimensional balanced solutions are found with dynamical model outputs as well as aircraft reconnaissance combined with diabatic heating derived from microwave rainfall rate retrievals. This work uses solutions from both datasets to make short-range intensity predictions. The results show that for the one-dimensional solutions, the tangential tendency does not match the dynamical model or aircraft wind tendencies. To relax the assumptions of the one-dimensional solutions to the geopotential tendency, solutions for idealized vortices are examined by finding two-dimensional solutions to the transverse circulation. The two-dimensional solutions allow for evaluation of the axisymmetric structure of the vortex on the (r, z)-plane without setting the baroclinicity to zero and the static stability to a constant value. While the sensitivity of tangential wind tendency to

diabatic forcing and the region of high inertial stability is more realistic in the two-dimensional results, the solutions still neglect the influence of friction from the boundary layer.

To understand further the role of frictional forcing in the boundary layer, two analytical slab models developed in this study provide insight into recent work that demonstrates how dry dynamics plays a role in determining eyewall location and size, how potential vorticity rings develop, and how an outer concentric eyewall forms through boundary layer "shock-like" structures. The analytical models show that when horizontal diffusion is neglected, the $u(\partial u/\partial r)$ term in the radial equation of motion and the $u[f + (\partial v/\partial r) + (v/r)]$ term in the tangential equation of motion develop discontinuities in the radial and tangential wind, with associated singularities in the boundary layer pumping and the boundary layer vorticity. The analytical models provide insight into the boundary layer processes that are responsible for determining the location of the eyewall and the associated diabatic heating that ultimately impacts the intensity of the tropical cyclone. This work shows that future research linking the roles of frictional forcing in the boundary layer to the diabatic forcing aloft while using a balanced model will be important for gaining insight into forcing effects on tropical cyclone intensity.

ACKNOWLEDGMENTS

DEDICATION

This work is dedicated to my mother, father, and aunt.

Without their continued love and support,

none of this would have been possible.

TABLE OF CONTENTS

LIST OF TABLES

LIST OF FIGURES

CHAPTER 1

INTRODUCTION

Understanding tropical cyclone intensity change, along with rapid intensification, has received

greater attention in recent years, especially through programs like the Hurricane Forecast Improve-

ment Project (Toepfer et al. 2010). While tropical cyclone prediction has improved, especially with

storm track, maximum wind intensity forecasts have lagged. Current techniques have been ineffec-

tive at predicting rapid intensification, e.g. a 30 kt or greater increase in intensity within a 24-hour

period. Traditionally, statistical-dynamical techniques have outperformed numerical weather pre-

diction models in forecasting intensity. Kaplan et al. (2010) find slowed improvements in statistical

intensity forecasting techniques since the early 2000s. To add to our understanding of tropical cy-

clone intensity and improve current forecasting methods, a deeper understanding of the tropical

cyclone transverse circulation during the life cycle of the tropical cyclone needs researching.

Ooyama (1969a) and Ooyama (1969b) show the first successful numerical simulations of the

life cycle of a tropical cyclone. As seen in Fig. 1.1, the vertical velocity, w, out of the boundary

layer is located outside the radius of maximum wind V_1. As noted by Vigh and Schubert (2009) and

Musgrave et al. (2012), the radial distance between the diabatic heating and the radius of maximum

wind determines the intensity change of the barotropic vortex. These studies indicate that in order

to improve forecasts of intensity change, the position of the diabatic heating must be correctly

simulated. Returning to evaluating the Ooyama model, one glaring issue is the formulation of the

boundary layer, the lowest of the three layers used in the model (Fig. 1.2). The model neglects

the $u \, (\partial u / \partial r)$ term in the boundary layer radial momentum equation. Ooyama (1969b) notes that

"frictionally-induced radial inflow may become so strong in an intense cyclone that the omission

of advection terms in (1) is not justifiable," where equation (1) refers to the gradient wind equation.
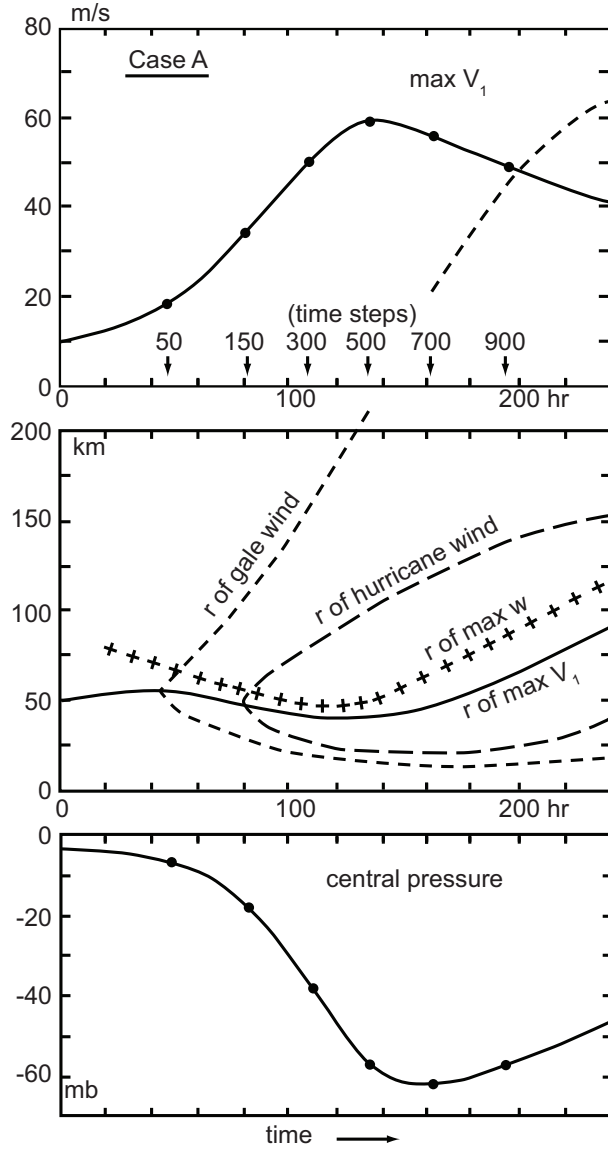
FIG. 1.1. A reproduction of Fig. 4 from Ooyama (1969a) depicting the time evolution of a numerically simulated tropical cyclone in which the boundary layer is assumed to be in gradient balance (the $u(\partial u/\partial r)$ term of the radial momentum equation is neglected in the boundary layer). The top panel shows the maximum tangential wind (max V_1) and a continuation of the radius of gale force wind from the middle panel; the middle panel shows the radii of maximum wind (max V_1), hurricane force wind, gale force wind, and maximum vertical velocity (w); and the bottom panel shows the central surface pressure. In the figure, max V_1 is the maximum tangential velocity, r represents radius, and w is the vertical velocity. The radius of gale wind extends into the upper plot.
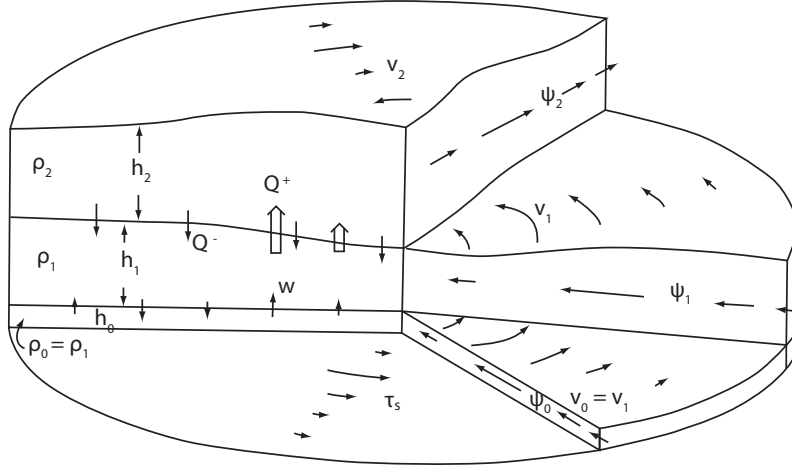
FIG. 1.2. The reproduction of Fig. 1 from Ooyama (1969a) shows the basic design of a three-layer, gradient balanced, axisymmetric hurricane model that contains moisture in the boundary layer. In the figure, ρ is the density of each layer, h is the depth of the layer, Q is the diabatic flux, τ_s is the tangential component of the shearing stress at the sea surface, v is the tangential component of the velocity, ψ is the radial mass flux, and w is the vertical component of the velocity.

In Fig. 1.3, Ooyama shows that the tangential velocity and vertical velocity shift radially inward with inclusion of the advection terms in the radial momentum equation. Also seen is a shift in the vertical velocity's proximity to the radius of maximum tangential wind. Because of these changes in the tropical cyclone structure, several questions result: How does the intensity change in a baroclinic vortex similar to that modeled by Ooyama? How do boundary layer frictional effects with the advection term in the radial momentum equation influence the placement of the vertical momentum flux out of the boundary? This thesis seeks to enhance the understanding of how diabatic heating affects intensity in a baroclinic vortex due to the shift in the radial location of the diabatic heating and develop analytical models to study the importance of the radial advection term, $u\,\partial u/\partial r$, in the slab boundary layer model.

The thesis follows this structure. Chapter 2 presents applications of the balanced vortex model. In this chapter, the transverse circulation and geopotential tendency equations show intensity

changes resulting from diabatic heating. Chapter 3 presents shock-like structures in the tropi-

cal cyclone boundary layer resulting from the radial advection term and frictional effects. In this

chapter, an analytical model explains shock formation. Chapter 4 offers a summary of the results

from the work in addition to a discussion that links the presented topics. At the end of the the-

sis, several appendices include additional information and results related to the work presented in

chapters 2 and 3.
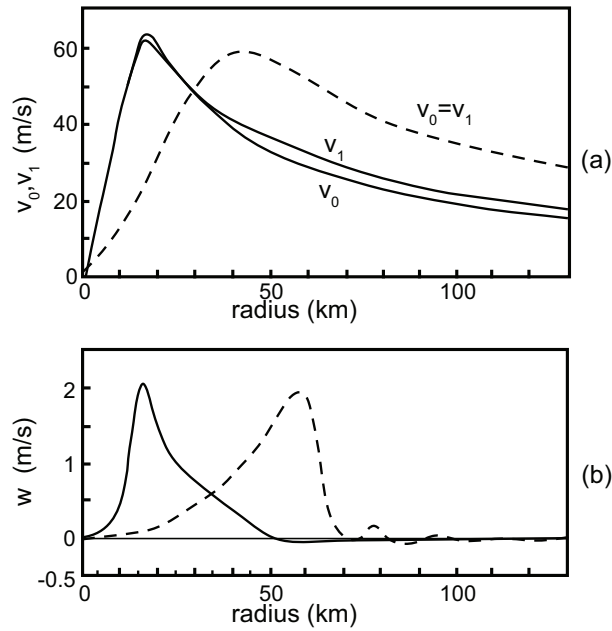
FIG. 1.3. The azimuthal profile of boundary layer tangential wind, v_0, and the lower layer tangential wind, v_1, for Model I (dashed) and Model II (solid) shown in the upper panel. The azimuthal distribution of the vertical velocity, w, at the top of the boundary layer for Model I (dashed) and Model II (solid) shown in the lower panel. Both figures are for $t = 146$ hours. This figure is adapted from Ooyama (1969b).

CHAPTER 2

SOLUTIONS OF THE TRANSVERSE CIRCULATION AND GEOPOTENTIAL TENDENCY

EQUATIONS

2.1. INTRODUCTION

To answer how the vortex responds to diabatic heating during the life cycle of a tropical cyclone, we return to Fig. 1.1, which shows that the radius of maximum Ekman pumping (depicted as r of max w) remains outside of the radius of maximum tangential velocity (depicted as r of max V_1). This relationship is known to indicate that the strongest diabatic heating occurs outside or near the radius of maximum tangential wind. In the context of the balanced vortex model, Musgrave et al. (2012) show how moving the region of strongest diabatic heating closer to the region of high inertial stability causes a stronger tangential velocity tendency response in the vortex. In fact, the response is extremely sensitive to radial shifts in the region of diabatic heating. In addition to work with the balanced vortex model, full physics models have been used to assess similar diabatic heating responses. These studies discuss the role of diabatic heating outside of the eyewall and in spiral rainbands (Wang 2009; Xu and Wang 2010; Fudeyasu and Wang 2011) and the role of eyewall tilt (Wang 2008b; Pendergrass and Willoughby 2009).

This work evaluates applying the concepts of Musgrave et al. (2012) to observed tropical cyclones by comparing one-dimensional solutions of the transverse circulation to two-dimensional solutions that have relaxed some of the vertical structure approximations used in the balanced vortex model formulated by Musgrave et al. (2012).

2.2. BALANCED VORTEX MODEL

Eliassen (1951) first solved the balanced vortex model using quasi-static theory to explain the response of the meridional circulation in a circular vortex to diabatic heating. The solutions for the meridional circulation can be applied to the tropical cyclone (Ooyama 1969a; Willoughby 1979; Vigh and Schubert 2009; Musgrave et al. 2012). We begin by defining the balanced vortex model in a similar method as presented by Vigh and Schubert (2009) and Musgrave et al. (2012). We consider inviscid, axisymmetric, quasi-hydrostatic, gradient balanced motions of a stratified, compressible atmosphere on an f-plane. We use log-pressure as the vertical coordinate by defining z as $H \ln(p_0/p)$, where $p_0 = 900$ hPa is the top of the boundary layer and $H = R_d T_0/g \approx 8.61$ km is the constant scale height, with R_d denoting the gas constant for dry air, $T_0 = 294.25$ K the constant reference temperature [based on the TOGA/COARE mean sounding (Lin and Johnson 1996)] and g the acceleration of gravity. The governing equations for the balanced vortex model are

$$\left(f + \frac{v}{r}\right) v = \frac{\partial \phi}{\partial r}, \tag{2.1}$$

$$\frac{\partial v}{\partial t} + u\left(f + \frac{\partial(rv)}{r\partial r}\right) + w\frac{\partial v}{\partial z} = 0, \tag{2.2}$$

$$\frac{\partial \phi}{\partial z} = \frac{g}{T_0}T, \tag{2.3}$$

$$\frac{\partial(ru)}{r\partial r} + \frac{\partial(\rho w)}{\rho\,\partial z} = 0, \tag{2.4}$$

$$\frac{\partial T}{\partial t} + u\frac{\partial T}{\partial r} + w\left(\frac{\partial T}{\partial z} + \frac{R_d T}{c_p H}\right) = \frac{Q}{c_p}, \tag{2.5}$$

where u and v are the radial and azimuthal components of velocity, w is the vertical log-pressure velocity, ϕ is the geopotential, $f = 5 \times 10^{-5}$ s^{-1} is the constant Coriolis parameter, $\rho(z) = \rho_0 e^{-z/H}$ is the pseudo-density, $\rho_0 = p_0/(R_d T_0) \approx 1.066$ kg m^{-3} is the constant reference density, and Q is

the diabatic heating. Regarding Q as known and/or parameterized, (2.1)–(2.5) constitute a closed system in u, v, w, ϕ, T, all of which are functions of (r, z, t). For the purposes of developing solutions to the balanced vortex model, we will provide initial vortex tangential velocity structure, v, as well as diabatic heating, Q/c_p, in order to retrieve the tangential velocity tendency, $(\partial v/\partial t) = v_t$. v_t is interpreted as the intensity change in the tropical cyclone caused by diabatic heating.

Using the hydrostatic equation (2.3) in (2.5) and using the gradient wind equation (2.1) in (2.2), we obtain

$$\frac{\partial \phi_t}{\partial z} + A\rho w - B\rho u = \frac{g}{c_p T_0} Q, \tag{2.6}$$

$$\frac{\partial \phi_t}{\partial r} - B\rho w + C\rho u = 0, \tag{2.7}$$

where $\phi_t = \partial \phi/\partial t$ is the geopotential tendency and where the static stability, A, the baroclinicity, B, and the inertial stability, C, are defined by

$$\rho A = \frac{g}{T_0} \left(\frac{\partial T}{\partial z} + \frac{R_d T}{c_p H} \right), \tag{2.8}$$

$$\rho B = -\frac{g}{T_0} \frac{\partial T}{\partial r} = -\left(f + \frac{2v}{r} \right) \frac{\partial v}{\partial z}, \tag{2.9}$$

$$\rho C = \left(f + \frac{2v}{r} \right) \left(f + \frac{\partial (rv)}{r \partial r} \right). \tag{2.10}$$

2.3. TRANSVERSE CIRCULATION EQUATION

Eliminating ϕ_t between (2.6) and (2.7) yields the transverse circulation equation given below as

$$\frac{\partial}{\partial r} \left(A \frac{\partial (r\psi)}{r \partial r} + B \frac{\partial \psi}{\partial z} \right) + \frac{\partial}{\partial z} \left(B \frac{\partial (r\psi)}{r \partial r} + C \frac{\partial \psi}{\partial z} \right) = \frac{g}{c_p T_0} \frac{\partial Q}{\partial r}, \tag{2.11}$$

where we have used the continuity equation, (2.4), to express the radial and vertical velocity components in terms of the streamfunction ψ as

$$\rho u = -\frac{\partial \psi}{\partial z} \quad \text{and} \quad \rho w = \frac{\partial (r\psi)}{r \partial r}. \tag{2.12}$$

The transverse circulation equation was first presented by Eliassen (1951) for the case where $\partial Q / \partial r$ is localized. The Green's function solutions demonstrate how the shape and strength of the transverse circulation depend on the coefficients A, B, and C. Vigh and Schubert (2009) highlight that Eliassen's approach has the following disadvantages: (i) the effects of the top and bottom boundary conditions and the circular geometry are not included, (ii) the important spatial variability of the inertial stability coefficient C is not included, and (iii) the diabatic heating is localized in z. The work presented here removes these limitations, as will be shown in section 2.5.

2.4. GEOPOTENTIAL TENDENCY EQUATION

As an alternative to defining the transverse circulation equation, we can proceed from (2.6) and (2.7) to obtain an equation for ϕ_t by eliminating u and w. First, we eliminate w to obtain

$$A\frac{\partial \phi_t}{\partial r} + B\frac{\partial \phi_t}{\partial z} + (AC - B^2)\rho u = \frac{g}{c_p T_0} BQ. \tag{2.13}$$

Next, we eliminate u to obtain

$$B\frac{\partial \phi_t}{\partial r} + C\frac{\partial \phi_t}{\partial z} + (AC - B^2)\rho w = \frac{g}{c_p T_0} CQ. \tag{2.14}$$

8

Now, using mass continuity defined by (2.4), we can eliminate u and w between equations (2.13) and (2.14) to obtain

$$\frac{\partial}{r\partial r}\left(r\frac{A}{D}\frac{\partial\phi_t}{\partial r} + r\frac{B}{D}\frac{\partial\phi_t}{\partial z}\right) + \frac{\partial}{\partial z}\left(\frac{B}{D}\frac{\partial\phi_t}{\partial r} + \frac{C}{D}\frac{\partial\phi_t}{\partial z}\right) = \frac{g}{c_pT_0}\left[\frac{\partial}{r\partial r}\left(r\frac{B}{D}Q\right) + \frac{\partial}{\partial z}\left(\frac{C}{D}Q\right)\right],$$

(2.15)

where $D = AC - B^2$.

The geopotential tendency equation is still a second-order partial differential equation with the same variable coefficients A, B, and C. Vigh and Schubert (2009) depict (2.15) as preferable if vortex evolution is the focus of understanding.

2.5. MODELS

In the following discussion in which we use the transverse circulation equation and the geopotential tendency equation, we consider cases in which $A > 0$, $C > 0$, and $D = AC - B^2 > 0$, so that the transverse circulation problem (2.11) is elliptic. If any of the conditions above are violated, the system is no longer elliptic and the methods to develop solutions to the geopotential tendency and transverse circulation equations are invalid. The condition $AC - B^2 > 0$ can also be interpreted as potential vorticity, $P > 0$, since

$$AC - B^2 = \frac{g}{\rho_0 T_0}e^{z/(\gamma H)}\left(f + \frac{2v}{r}\right)P,$$

(2.16)

where $\gamma = c_p/c_v$ is the ratio of the specific heats and the potential vorticity is given by

$$P = \frac{1}{\rho}\left[-\frac{\partial v}{\partial z}\frac{\partial \theta}{\partial r} + \left(f + \frac{\partial(rv)}{r\partial r}\right)\frac{\partial \theta}{\partial z}\right].$$

(2.17)

To study elliptic solutions, we will show results with two models. The first finds one-dimensional solutions to the geopotential tendency. This one-dimensional model, based on an elliptic solver by Fulton (2011), is similar to that developed by Musgrave et al. (2012). The solver provides a fast, simple approach for evaluating the effects of diabatic heating on the vortex intensity due to its numerous assumptions. The second model uses a successive over-relaxation iterative method to find the two-dimensional solutions of the transverse circulation. This approach relaxes a number of the assumptions used by Musgrave et al. (2012).

2.5.1. ONE-DIMENSIONAL BALANCED SOLUTIONS

For the one-dimensional balanced solutions, we begin by setting the baroclinicity, B, to zero and defining the static stability and inertial stability as

$$N^2 = \rho A = \frac{g}{T_0} \left(\frac{\partial T}{\partial z} + \frac{RT}{c_p H} \right), \tag{2.18}$$

$$\hat{f}^2 = \rho C = \left(f + \frac{2v}{r} \right) \left(f + \frac{\partial (rv)}{r \partial r} \right). \tag{2.19}$$

From these assumptions, equations (2.6) and (2.7) become

$$\frac{\partial \phi_t}{\partial z} + N^2 w = \frac{g}{c_p T_0} Q \tag{2.20}$$

and

$$\frac{\partial \phi_t}{\partial r} + \hat{f}^2 u = 0. \tag{2.21}$$

10

Following the same steps to obtain (2.15) by eliminating u and w between equation (2.20) and (2.21), the geopotential tendency equation becomes

$$N^2 \frac{\partial}{r \partial r}\left(\frac{r}{\hat{f}^2}\frac{\partial \phi_t}{\partial r}\right) + \left(\frac{\partial}{\partial z} - \frac{1}{H}\right)\frac{\partial \phi_t}{\partial z} = \frac{g}{c_p T_0}\left(\frac{\partial}{\partial z} - \frac{1}{H}\right)Q. \tag{2.22}$$

To evaluate elliptic solutions of (2.22), we assume $\hat{f}N > 0$ everywhere.

Musgrave et al. (2012) show that through the boundary conditions,

$$\frac{\partial \phi_t}{\partial z} = 0 \text{ at } z = 0, \ z_t, \tag{2.23}$$

and vertical structure through the separation of variables,

$$\begin{pmatrix} Q(r,z) \\ T_t(r,z) \\ w(r,z) \end{pmatrix} = \begin{pmatrix} \hat{Q}(r) \\ \hat{T}_t(r) \\ \hat{w}(r) \end{pmatrix} \exp\left(\frac{z}{2H}\right)\sin\left(\frac{\pi z}{z_T}\right),$$

$$\begin{pmatrix} \phi_t(r,z) \\ v_t(r,z) \\ u(r,z) \end{pmatrix} = \begin{pmatrix} \hat{\phi}_t(r) \\ \hat{v}_t(r) \\ \hat{u}(r) \end{pmatrix} \exp\left(\frac{z}{2H}\right)\left[\cos\left(\frac{\pi z}{z_T}\right) - \frac{z_T}{2\pi H}\sin\left(\frac{\pi z}{z_T}\right)\right], \tag{2.24}$$

the hydrostatic, gradient wind, tangential wind, and thermodynamic equations imply that

$$\frac{g}{T_0}\hat{T}_t(r) = -\frac{z_T}{\pi}\left(\frac{\pi^2}{z_T^2} + \frac{1}{4H^2}\right)\hat{\phi}_t(r), \tag{2.25}$$

$$\hat{v}_t(r) = \left(f + \frac{2v}{r}\right)^{-1}\frac{d\hat{\phi}_t(r)}{dr}, \tag{2.26}$$

$$\hat{u}(r) = -\hat{f}^{-2}\frac{d\hat{\phi}_t(r)}{dr}, \tag{2.27}$$

$$\hat{w}(r) = \frac{g}{T_0 N^2}\left(\frac{\hat{Q}(r)}{c_p} - \hat{T}_t(r)\right). \tag{2.28}$$

Shown in Fig. 2.1, the vertical structure functions, (2.24), represent typical structures of Q, T_t, w, ϕ_t, v, and u. Substituting (2.24) into (2.22), Musgrave et al. (2012) show that the ordinary differential equation for the radial structure of the temperature tendency is

$$\hat{T}_t - \frac{d}{rdr}\left(\ell^2 r\frac{d\hat{T}_t}{dr}\right) = \frac{\hat{Q}}{c_p},$$

$$\frac{d\hat{T}_t}{dr} = 0 \quad \text{at } r = 0, \tag{2.29}$$

$$\frac{d\hat{T}_t}{dr} = -\left(\frac{K_1(b/\ell_0)}{\ell_0 K_0(b/\ell_0)}\right)\hat{T}_t \quad \text{at } r = b,$$

where the Rossby length is defined as

$$\ell(r) = \frac{N}{\hat{f}(r)}\left(\frac{\pi^2}{z_T^2} + \frac{1}{4H^2}\right)^{-1/2} = \frac{f}{\hat{f}(r)}\ell_0. \tag{2.30}$$

ℓ_0 is the constant far-field value, which we shall assume is equal to 1000 km, K_0 and K_1 are modified Bessel functions, and $\hat{f}$ is the effective Coriolis parameter. After solving (2.29) for $\hat{T}_t$, we can use (2.24) to recover the fields $T_t(r, z)$, $v_t(r, z)$, $\phi_t(r, z)$, $u(r, z)$, and $w(r, z)$.
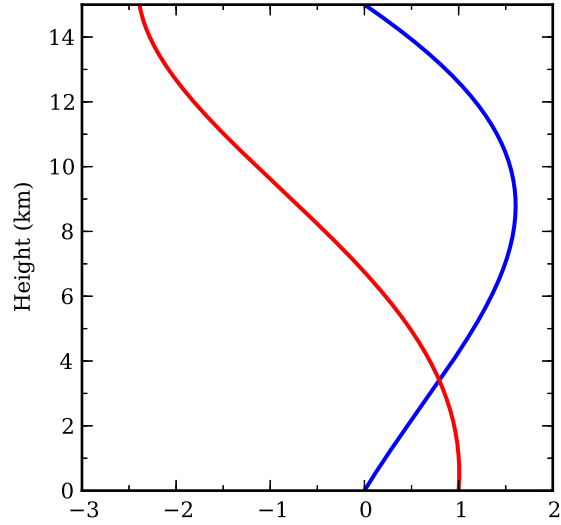
FIG. 2.1. The vertical structure functions in (2.24) are $\exp[z/2H]\sin(\pi z/z_T)$ (blue) and $\exp[z/2H]\{\cos(\pi z/z_T) - [z_T/(2\pi H)]\sin(\pi z/z_T)\}$ (red). The maximum of the blue curve reaches an approximate value of 1.606 at $z = 8.798$ km.

To show an idealized case of a specified vortex to diabatic heating through the geopotential tendency equation, we will use a similar vortex as described by Musgrave et al. (2012) that we will define as

$$v(r) = \frac{1}{c_r c_v} \frac{r_m v_m}{r} \left[1 - \exp\left(-\frac{r^2 c_r^2}{r_m^2} \right) \right], \tag{2.31}$$

where v_m is the maximum tangential velocity and r_m is the radius of maximum v_m. c_r and c_v are constants respectively defined as 1.209 and 0.63817. Now, we define the diabatic heating in an annular ring (Eliassen 1971; Eliassen and Lystad 1977; Yamasaki 1977; Emanuel 1997; Smith and Vogl 2008; Smith and Montgomery 2008; Kepert 2010a,b). The annular ring of diabatic heating represents the response in nature to the maximum vertical velocity at the top of the boundary layer. (2.1)–(2.5) in section 2.2 do not contain a boundary layer. However, the effects of the boundary

13

layer vertical velocity can be represented by specifying the heating as

$$
\hat{Q}(r) = \hat{Q}_{ew}
\begin{cases}
0 & 0 \leq r \leq r_1, \\[2mm]
S\left(\frac{r_2 - r}{r_2 - r_1}\right) & r_1 \leq r \leq r_2, \\[2mm]
1 & r_2 \leq r \leq r_3, \\[2mm]
S\left(\frac{r - r_3}{r_4 - r_3}\right) & r_3 \leq r \leq r_4, \\[2mm]
0 & r_4 \leq r < \infty,
\end{cases}
\tag{2.32}
$$

where $S(s) = 1 - 3s^2 + 2s^3$ is a cubic interpolating function and r_1, r_2, r_3, and r_4 are specified constants defining width and shape of the diabatic heating profile. r_1 and r_2 define the inner region of the heating where r_3 and r_4 define the outer portion of the heating. The eyewall diabatic heating, $\hat{Q}_{ew}$, is defined as

$$
\frac{\hat{Q}_{ew}}{c_p} = G \frac{\hat{Q}_0}{c_p},
\tag{2.33}
$$

where $\hat{Q}_0/c_p = 3.2$ K day^{-1} and the dimensionless geometric factor G is given by

$$
G = \frac{10 \ (250 \ \text{km})^2}{(3r_3^2 + 4r_3 r_4 + 3r_4^2) - (3r_1^2 + 4r_1 r_2 + 3r_2^2)}.
\tag{2.34}
$$

A discussion on deriving G is found in Musgrave et al. (2012). Table 2.1 contains the parameters used for (2.32) for three of the cases shown by Musgrave et al. (2012) with a vortex where $v_m = 30$ m s^{-1} and $r_m = 30$ km (shown in Fig. 2.2). The response to the diabatic heating is shown in Fig. 2.3. In all three cases, the integrated kinetic energy of the storm (not shown) increases. However, the response of case H1 does not change the maximum tangential velocity. As the heating moves inward towards the region of high inertial stability, the maximum tangential velocity of the tropical cyclone increases and is relocated to the region containing the heating.

14

TABLE 2.1. The bounding radii, r_1, r_2, r_3, r_4, and the geometrical factor, G, used by Musgrave et al. (2012) for their first three cases (H1 – H3). G is computed using (2.34).

Case	r_1 (km)	r_2 (km)	r_3 (km)	r_4 (km)	G
H1	40	45	55	60	41.67
H2	30	35	45	50	52.08
H3	20	25	35	40	69.44
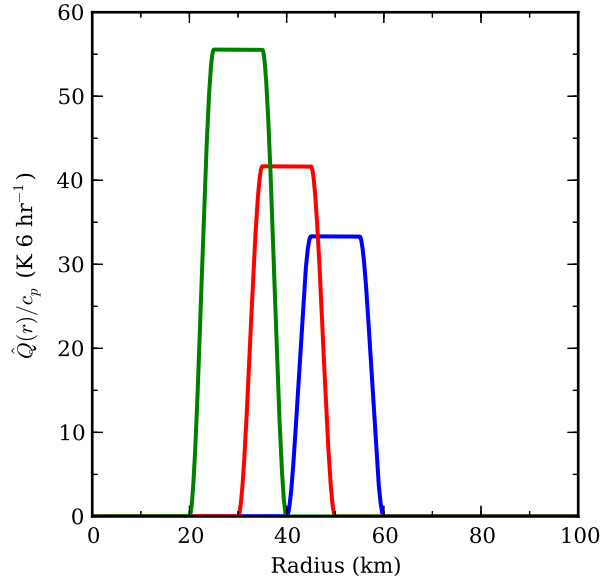
FIG. 2.2. The diabatic forcing, $\hat{Q}/c_p$, for cases H1 – H3 based on the parameters in Table 2.1. Case H1 is shown in blue, case H2 in red, and case H3 in green.

Slocum (2012) found one-dimensional balanced solutions of the geopotential tendency with output from the Hurricane Weather Research and Forecasting model (HWRF) for the Atlantic and Eastern Pacific ocean basins during 2011 (Gopalakrishnan and Coauthors 2011). For the experiment, Slocum (2012) used data extracted at 700 hPa, a typical flight level of hurricane aircraft reconnaissance. Since the HWRF model underwent mid-season changes, the sample used in the experiment is limited to 15 named storms in the Atlantic (05L to 19L) and 10 Eastern Pacific storms (06E to 13E). Fig. 2.4 depicts the response to the HWRF model diabatic heating based

15

on the large scale condensation heating output. The case uses initial conditions from the 78-hour HWRF forecast for Hurricane Irene on 1800 UTC 21 August 2011 with the 90-hour HWRF forecast as verification. The case shows that the solver effectively simulates the change in intensity predicted by the HWRF model.
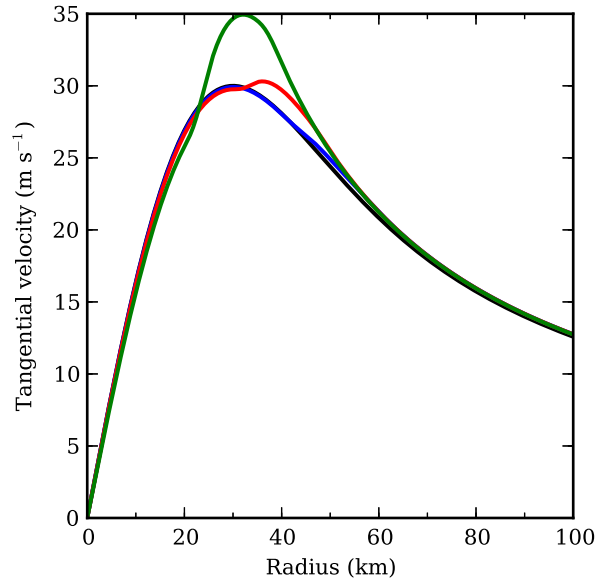
FIG. 2.3. The change in vortex structure due to diabatic heating. The blue curve shows the response to the parameters for H1 shown in row 1 of Table 2.1, the red curve shows the response to the parameters for H2 shown in row 2 of Table 2.1, and the green curve shows the response to the parameters for H3 shown in row 3 of Table 2.1. The black curve is the initial profile used for the model with a vortex where $v_m = 30$ m s^{-1} and $r_m = 30$ km.

While the response for this case in Hurricane Irene (2011) seems to indicate the one-dimensional balanced solutions can explain the tangential velocity response, Fig. 2.5 shows that the balanced solutions are unable to physically dissipate storms which results in overpredicting intensity. There are a few cases where weak negative diabatic heating in the HWRF output results in a negative tangential velocity tendency in otherwise dry regions. The cases in Fig. 2.5 that did dissipate the tropical cyclone either responded to a small region of negative diabatic heating output by HWRF

or other frictional effects neglected in the formulation of the one-dimensional balanced solutions. This dissipation was less than 1 m s^{-1}.
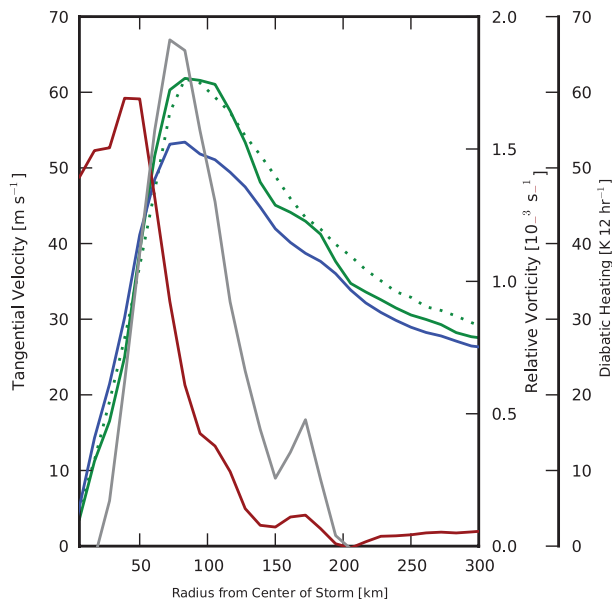
FIG. 2.4. Azimuthally averaged profiles of 700 hPa tangential velocity from the 78-hour HWRF forecast for Hurricane Irene on 1800 UTC 21 August 2011(blue), relative vorticity (red), and diabatic heating (gray) taken from the 78-hour HWRF forecast output. The profile of the 12-hour one-dimensional balanced solution response is shown in solid green and the HWRF 90-hour forecast tangential velocity is in dashed green.
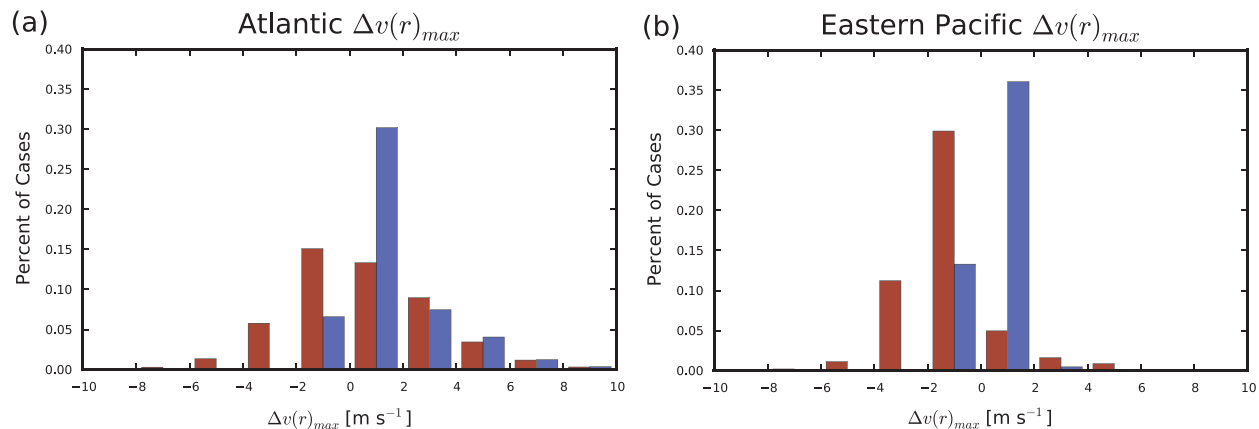
FIG. 2.5. Normalized histograms of the change in intensity for the Atlantic (a) and Eastern Pacific (b) 2011 Hurricane Season. The change in intensity is binned by 2 m s^{-1} from -10 to 10 m s^{-1}. HWRF is in red and the geopotential tendency equation response is in blue.

Since it is possible that HWRF does not respond to the diabatic forcing in the same manner as observed storms, the one-dimensional balanced solutions for the geopotential tendency are used with the NOAA Advanced Microwave Sounding Unit (AMSU) rain rate product from the NESDIS Operational Microwave Surface and Precipitation Products (Ferraro 1997; Ferraro et al. 2000) along with aircraft reconnaissance winds processed using a similar method to Knaff et al. (2011). Fig. 2.6 shows the maximum tangential velocity and radius of maximum winds for Hurricane Isaac (2012) using the aircraft reconnaissance winds.
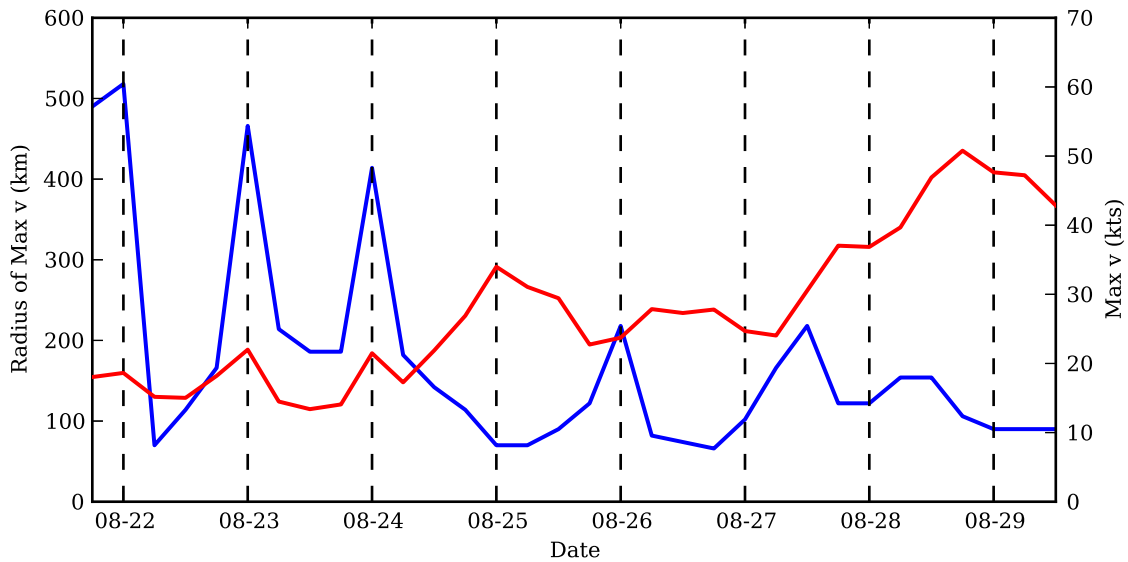
FIG. 2.6. The maximum symmetrically averaged winds (red) and radius of maximum wind (blue) for the life of Hurricane Isaac (2012) taken from aircraft reconnaissance data processed with the method of Knaff et al. (2011).

Fig. 2.7 shows that the 6-, 12-, 18-, and 24-hour predictions from the balanced solutions have a low mean error and absolute error. However, as indicated by the error bars, the standard deviation of all the cases is large so the figure does not show the full picture. Not shown is the change in tangential velocity to the observed intensity change. This relationship shows a very poor correlation and that persistence outperforms the one-dimemsional balanced solutions.
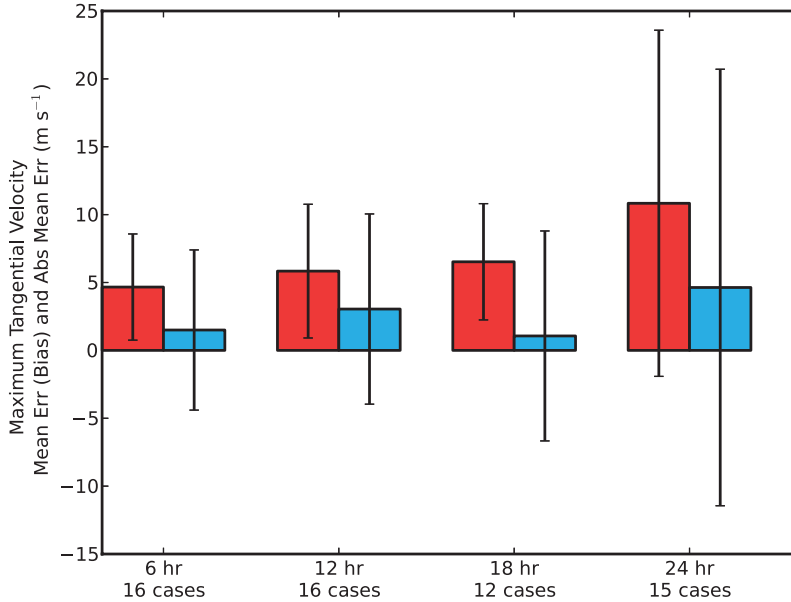
FIG. 2.7. The absolute error (red) and mean error [bias] (blue) for the 6-, 12-, 18-, and 24-hour predictions finding the one-dimensional balanced solutions with the NESDIS Operational Microwave Surface and Precipitation Products along with aircraft reconnaissance winds for the life of Hurricane Isaac (2012).

While the method can capture the actual tangential velocity tendency for a few observed storms, it shows similar issues are experienced with HWRF data. To compensate, several assumptions made in formulating the method for finding one-dimensional solutions to geopotential tendency must be relaxed.

2.5.2. Two-dimensional balanced solutions

While the one-dimensional elliptic solver for the geopotential tendency equation provides us with an analytical solution, it does have several limitations that manifest themselves during the application of the solver to observed data. To remove some of the limitations, we switch to a successive over-relaxation technique. The successive over-relaxation technique is an iterative method for solving the finite difference form of a partial differential equation. The successive over-relaxation technique's application to (2.11) is outlined in appendix A.3. A detailed discussion of how the technique works is provided in Haltiner and Williams (1980) and Stoer and Bulirsch (1980).

For the model, we use the domain $0 \leq r \leq 1200$ km and $0 \leq z \leq 30$ km with a grid spacing $\Delta r = 500$ m and $\Delta z = 100$ m. At the top boundary ($z = z_T$), we assume $w = 0$. While at the top of the boundary layer ($z = 0$), we assume that the boundary layer pumping is by $\psi(r, 0) = \psi_0(r)$, where $\psi_0(r)$ is a specified function.

$$\psi(r, 0) = \psi_0(r), \quad \psi(r, z_T) = 0, \tag{2.35}$$

$$\psi(0, z) = 0, \quad \text{and} \tag{2.36}$$

$$\frac{\partial \psi}{\partial r} = -\frac{\psi}{\ell} \quad \text{at} \quad r = r_B. \tag{2.37}$$

The specification of the lateral boundary condition (2.37) is less straightforward and is discussed in detail in appendix A.2.

In this section, the static, A, and inertial, C, stabilities are no longer constant. In addition, the baroclinicity, B, is non-zero. The stabilities are determined using equations (2.8) and (2.10) and the baroclinicity using (2.9).

For this study, we will specify a modified Rankine vortex. The modified Rankine vortex takes the form

$$v(r, z) = \frac{1}{2}\zeta_0(z) \begin{cases} r & 0 \leq r \leq r_m(z) \\ r_m^{\alpha+1}(z)/r^\alpha & r_m(z) \leq r < \infty, \end{cases} \tag{2.38}$$

where

$$r_m(z) = \left(\frac{f}{f + \zeta_0(z)}\right)^{1/2} R_0. \tag{2.39}$$

α and R_0 are specified constants, and $\zeta_0(z)$ is a specified function. From the definition $\frac{1}{2}fR^2 = rv + \frac{1}{2}fr^2$, it can be shown that $R(r_m(z), z) = R_0$, so the specification of R_0 is equivalent to the specification of the potential radius along the maximum wind in the (r, z)-plane. Fig. 2.8

20

shows a plot of $v(r, z)$ based on equations (2.38) and (2.39) using $f = 5 \times 10^{-5}$ s^{-1}, $R_0 \approx 192$ km, and $\zeta_0(z)$ as a cubic spline interpolation with $\zeta_0(0) = 40f$ and $\zeta_0(z_T) = -0.5f$. $v(r, z)$ is also smoothed by applying the nine point local smoother described in appendix A.1 for 100 iterations. The vortex is smoothed to remove roughness in the tangential velocity profile near r_m and eliminate the discontinuity in relative vorticity. This gives a profile where $r_m(0) \approx 30$ km and $v(r_m(0), 0) \approx 30$ m s^{-1}.
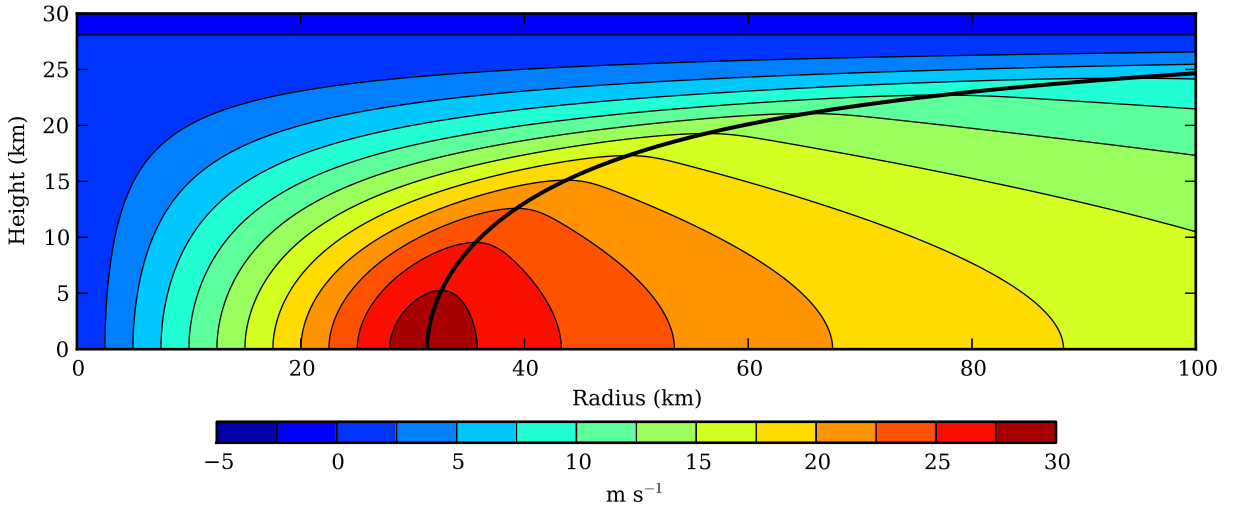
FIG. 2.8. A plot of the tangential velocity in the (r, z)-plane using $f = 5 \times 10^{-5}$ s^{-1} (contour), $R_0 \approx 192$ km (thick black line), and $\zeta_0(z)$ as a cubic b-spline with $\zeta_0(0) = 40f$ and $\zeta_0(z_T) = -0.5f$. This gives $v(r_m(0), 0) = 30$ m s^{-1}.

While other specified tangential velocity profiles could be used without applying the filter, the modified Rankine vortex provides us with the most flexibility in determining r_m and the maximum tangential velocity. The relative vorticity associated with (2.38) is

$$\zeta(r, z) = \zeta_0(z) \begin{cases} 1 & 0 \leq r \leq r_m(z) \\ \frac{1}{2}(1 - \alpha)[r_m(a)/r]^{1+\alpha} & r_m(z) \leq r < \infty. \end{cases} \tag{2.40}$$

21

As noted previously, there is a discontinuity of the relative vorticity at $r_m(z)$. The above equation is not used to actually calculate the relative vorticity since we want to remove the discontinuity through the nine point local smoother. Instead, after the tangential velocity profile is smoothed, the relative vorticity is calculated through

$$\zeta = \frac{\partial(rv)}{r\partial r}. \tag{2.41}$$

To calculate the temperature field, $T(r, z)$, we use an inward integration of the thermal wind equation

$$\frac{g}{T_0}\frac{\partial T}{\partial r} = \left(f + \frac{2v}{r}\right)\frac{\partial v}{\partial z}. \tag{2.42}$$

The outer boundary is set to a modified version of the temperature profile from the TOGA/COARE mean sounding (Lin and Johnson 1996). A modified version of the TOGA/COARE mean sounding (Lin and Johnson 1996) is used to provide the vertical structure of temperature for calculating the static stability. The TOGA/COARE mean sounding is modified so the static stability increases uniformly with height until reaching the tropopause. While substantially changing the lapse rate, the change allows for better performance when using a successive over-relaxation technique to find the two-dimensional solutions. Fig. 2.9 shows a Skew-T Log-P thermodynamic diagram with the TOGA/COARE mean sounding and the modified profile used here. Once the temperature profile is computed, the necessary information is gained to calculate the coefficients $A(r, z)$, $B(r, z)$, and $C(r, z)$ [shown in Fig. 2.10].
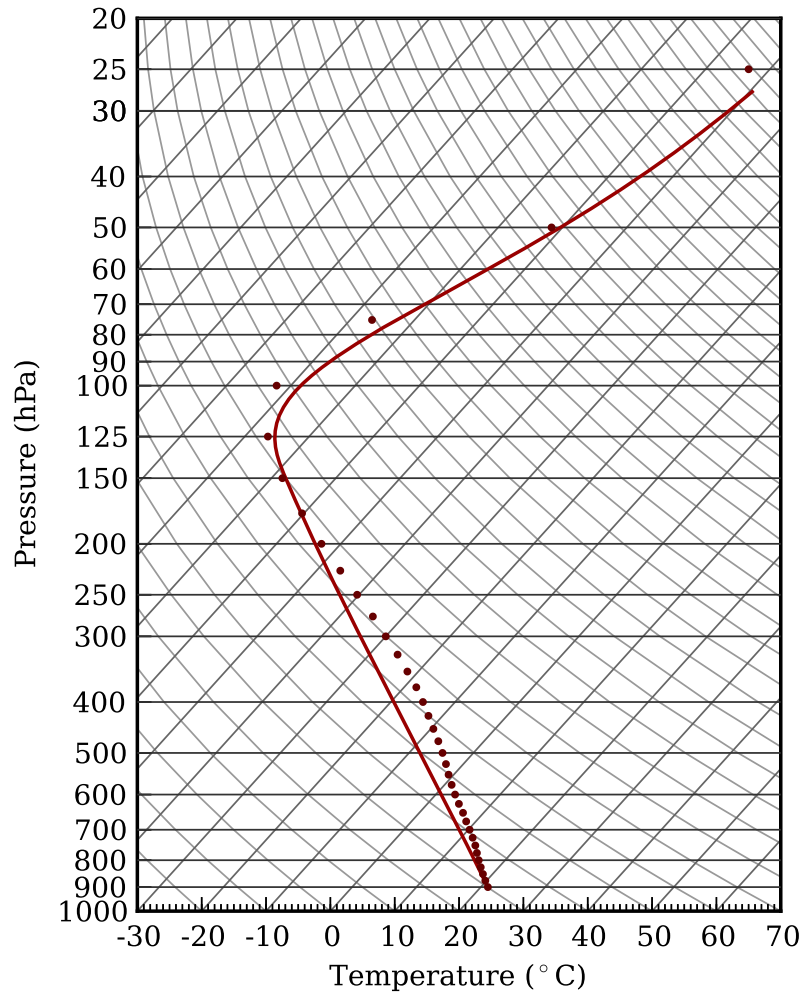
FIG. 2.9. The Skew-T Log-P thermodynamic diagram shows the TOGA/COARE mean temperature sounding (Lin and Johnson 1996) (red dots) along with the modified sounding used with the successive over-relaxation iterative method (solid red line). The modified sounding is plotted from $0 \leq z \leq 30$ km, where z refers to log-pressure height as defined in the text of section 2.2.
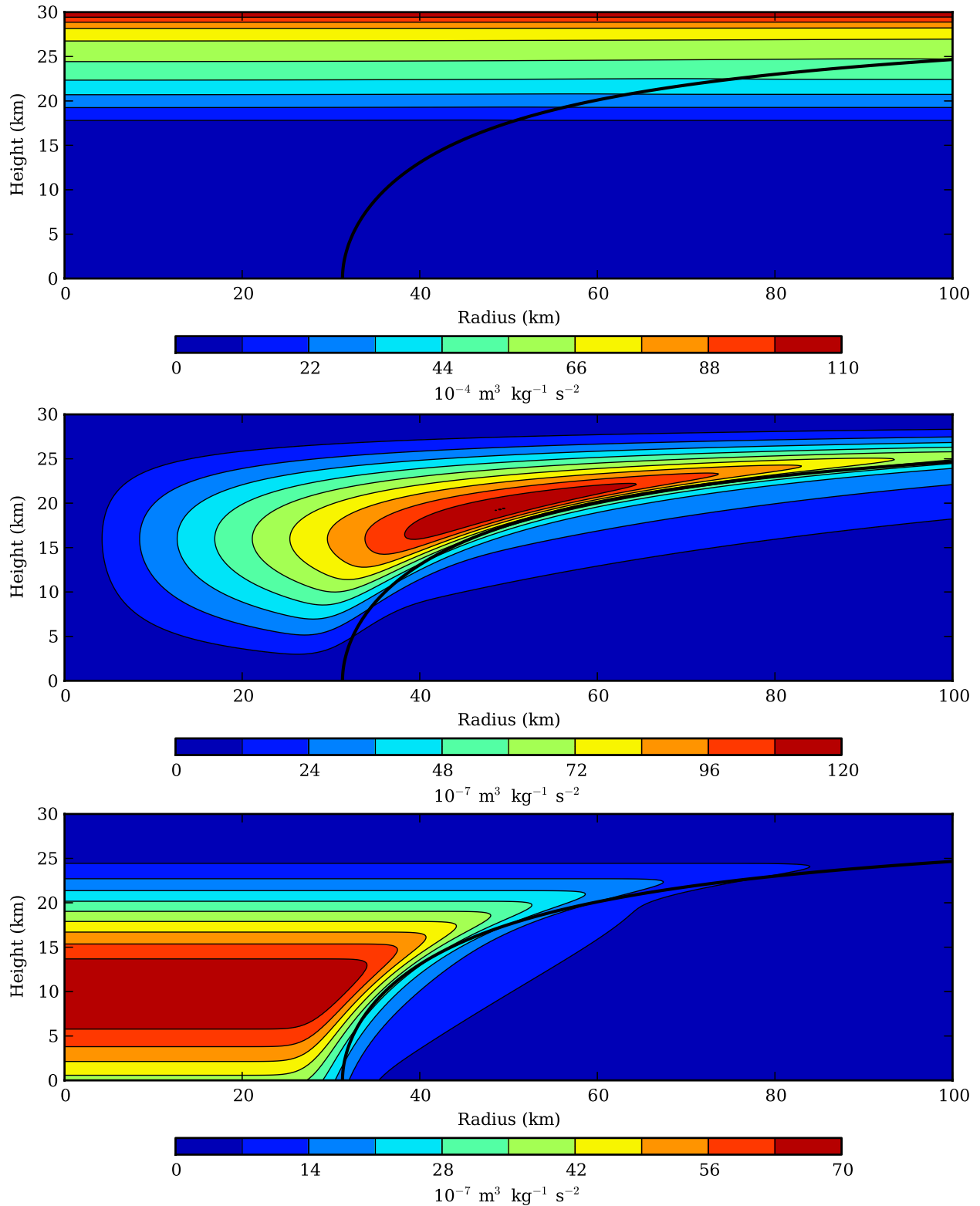
FIG. 2.10. The static stability, baroclinicity, and inertial stability shown on the (r, z)-plane for the domain $0 \leq z \leq 30$ km and $0 \leq r \leq 100$ km. A, B, and C are calculated using equations (2.8)–(2.10). The thick black line represents $R_0 \approx 192$ km, the potential radius associated with the maximum tangential velocity.

To specify the $Q(r, z)$ term in (2.11), we assume that the diabatic heating is confined to the troposphere and has the form of an outward sloping annular ring with smooth edges. The mathematical form is $Q(r, z) = 0$ for $z \geq 2z_{\max}$, while for $0 \leq z \leq 2z_{\max}$ the form is

$$Q(r, z) = Q_{\max} \sin^2 \left(\frac{\pi z}{2z_{\max}} \right) \begin{cases} 0 & 0 \leq r \leq r_1(z), \\ S \left(\dfrac{r_2(z) - r}{r_2(z) - r_1(z)} \right) & r_1(z) \leq r \leq r_2(z), \\ 1 & r_2(z) \leq r \leq r_3(z), \\ S \left(\dfrac{r - r_3(z)}{r_4(z) - r_3(z)} \right) & r_3(z) \leq r \leq r_4(z), \\ 0 & r_4(z) \leq r < \infty, \end{cases} \qquad (2.43)$$

where $S(s) = 1 - 3s^2 + 2s^3$ is the cubic interpolating function, $Q_{\max}$ and $z_{\max}$ are specified constants, and $r_1(z), r_2(z), r_3(z), r_4(z)$ are specified functions. We chose the central eyewall region to be 10 km wide and the two transition regions to be 5 km wide, so that

$$r_2(z) = r_1(z) + 5 \, \mathrm{km},$$

$$r_3(z) = r_1(z) + 15 \, \mathrm{km}, \qquad (2.44)$$

$$r_4(z) = r_1(z) + 20 \, \mathrm{km}.$$

For the calculations shown here we have used the following five choices for the function $r_1(z)$:

$$r_1(z) = r_m(z) + 20\,\text{km} \quad \text{(Case H1)},$$

$$r_1(z) = r_m(z) + 15\,\text{km} \quad \text{(Case H2)},$$

$$r_1(z) = r_m(z) + 10\,\text{km} \quad \text{(Case H3)}, \tag{2.45}$$

$$r_1(z) = r_m(z) + 5\,\text{km} \quad \text{(Case H4)},$$

$$r_1(z) = r_m(z) \quad \text{(Case H5)}.$$

The maximum eyewall diabatic heating, denoted by Q_{max}, is determined by imposing the constraint that the total diabatic heating at $z = z_{\text{max}} = 7.5$ km is fixed according to

$$2\pi \int_{r_1(z_{\text{max}})}^{r_4(z_{\text{max}})} \frac{Q(r, z_{\text{max}})}{c_p} r\,dr = \left(6.0\,\text{K day}^{-1}\right) \cdot \pi (250\,\text{km})^2. \tag{2.46}$$

For further discussion of this normalization technique, see Musgrave et al. (2012). Substituting (2.43) into (2.46), and performing the integration, we obtain

$$\frac{Q_{\text{max}}}{c_p} = G \cdot \left(6.0\,\text{K day}^{-1}\right), \tag{2.47}$$

where the dimensionless geometrical factor G is given by

$$G = \frac{10\,(250\,\text{km})^2}{\left(3r_3^2 + 4r_3 r_4 + 3r_4^2\right)_{z_{\text{max}}} - \left(3r_1^2 + 4r_1 r_2 + 3r_2^2\right)_{z_{\text{max}}}}, \tag{2.48}$$

with the subscript z_{max} indicating the functions in parentheses are to be evaluated at $z = z_{\text{max}}$. Note that $G = 1$ in the special case $r_1 = r_2 = 0$ and $r_3 = r_4 = 250$ km, in which case the peak value of the diabatic heating is $Q_{\text{max}}/c_p = 6.0\,\text{K day}^{-1}$, a value typical of western Pacific convective cloud

cluster regions (Yanai et al. 1973). Plots of $Q(r, z)/c_p$, computed using the parameters calculated through (2.45), are shown in Fig. 2.11 at $Q_{\max}$.
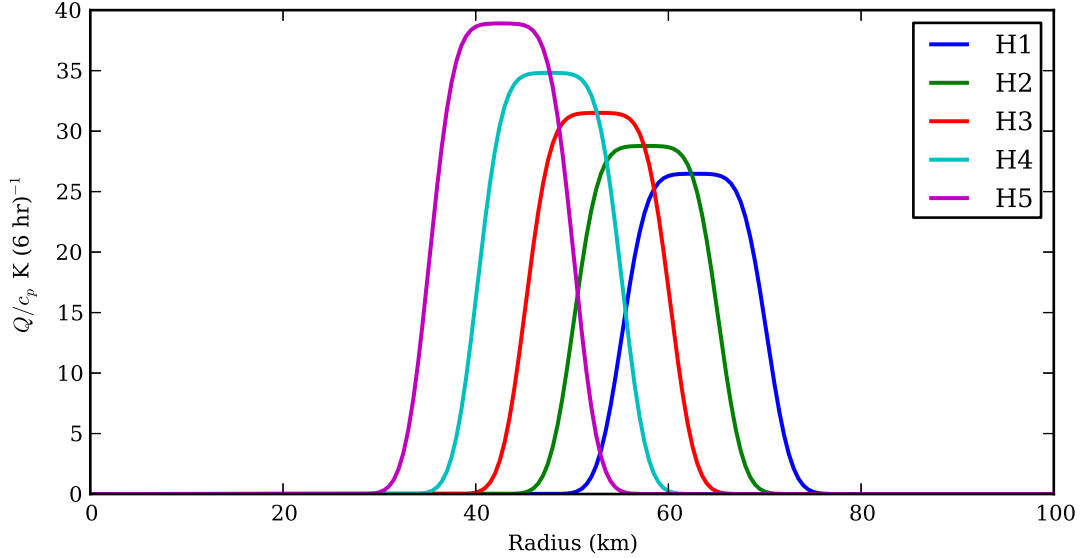
FIG. 2.11. The figure shows the region of strong diabatic heating, $Q_{\max}/c_p$, for the five cases described in equations (2.44) and (2.45). The magenta curve is case H1, the cyan curve is case H2, the red curve is case H3, the green curve is case H4, and the blue curve is case H5.

In all five cases, the maximum diabatic heating lies outside the radius of maximum wind. In case H5, a small amount of the diabatic heating falls inside the radius of maximum wind. Musgrave et al. (2012) show that the tangential velocity tendency response is unrealistic when the diabatic heating is in the region of high inertial stability so this case is not assessed in this work. Figs. 2.12–2.16 show Q/c_p, ψ, u, w, $\partial v/\partial t$, and $\partial T/\partial t$ on the (r, z)-plane for cases H1–H5. Fig. 2.17 shows the final tangential velocity for cases H1–H5 at $z = 2$ km.

27
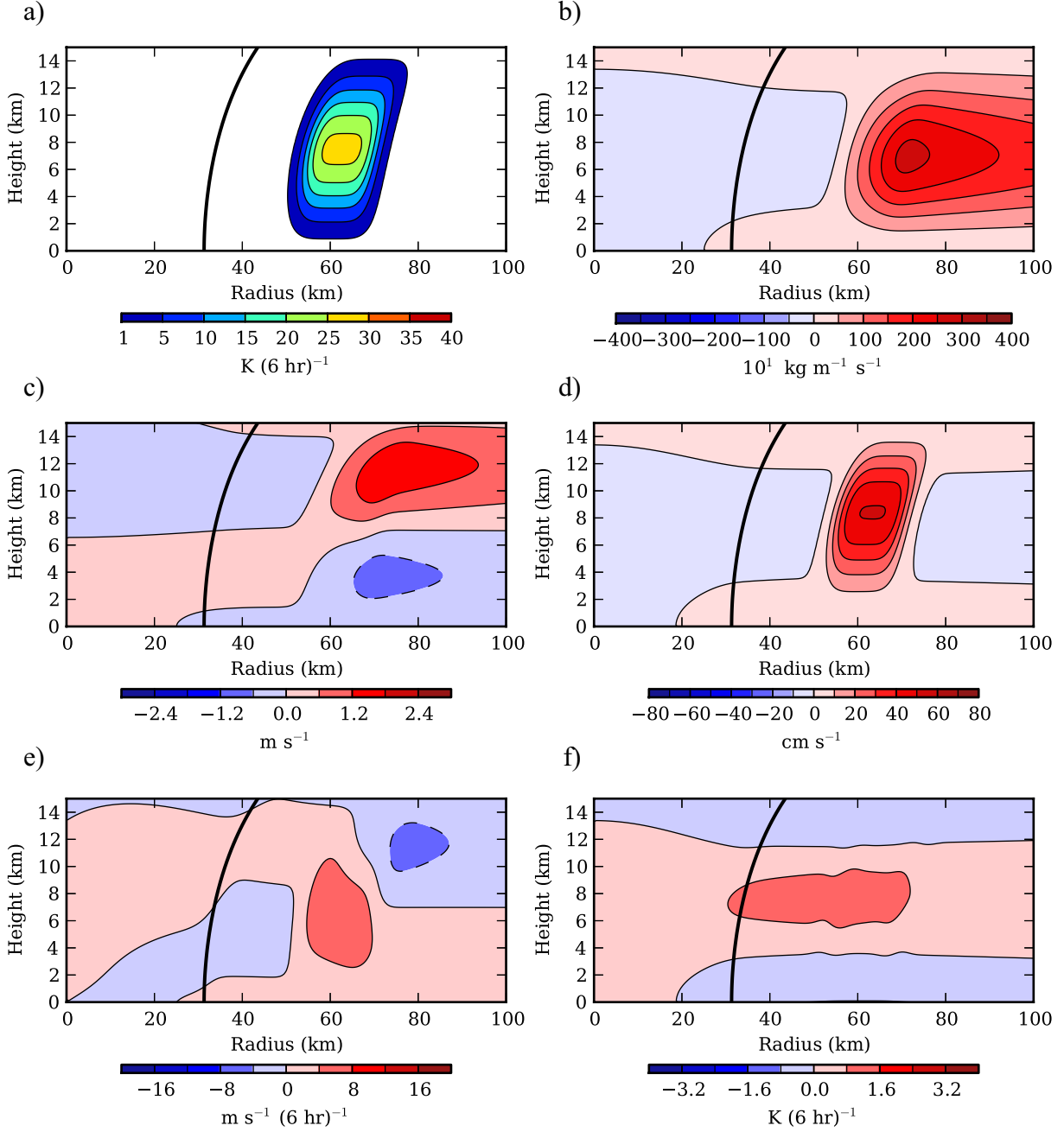
FIG. 2.12. Changes in vortex structure from the initial tangential velocity shown in Fig. 2.8 for the (r, z)-plane for case H1. The solutions assume the diabatic heating is applied for 6 hours. The upper left panel, a), is the diabatic heating; upper right panel, b), is ψ; middle left panel, c), is u; middle right panel, d), is w; lower left panel, e), is $\partial v/\partial t$; and lower right panel, f), is $\partial T/\partial t$. Each panel has a thick black line representing $R_0 \approx 192$ km, the potential radius surface associated with the maximum tangential velocity. Only the lower half of the model domain is shown for $0 \leq r \leq 100$ km here and in the following four figures.
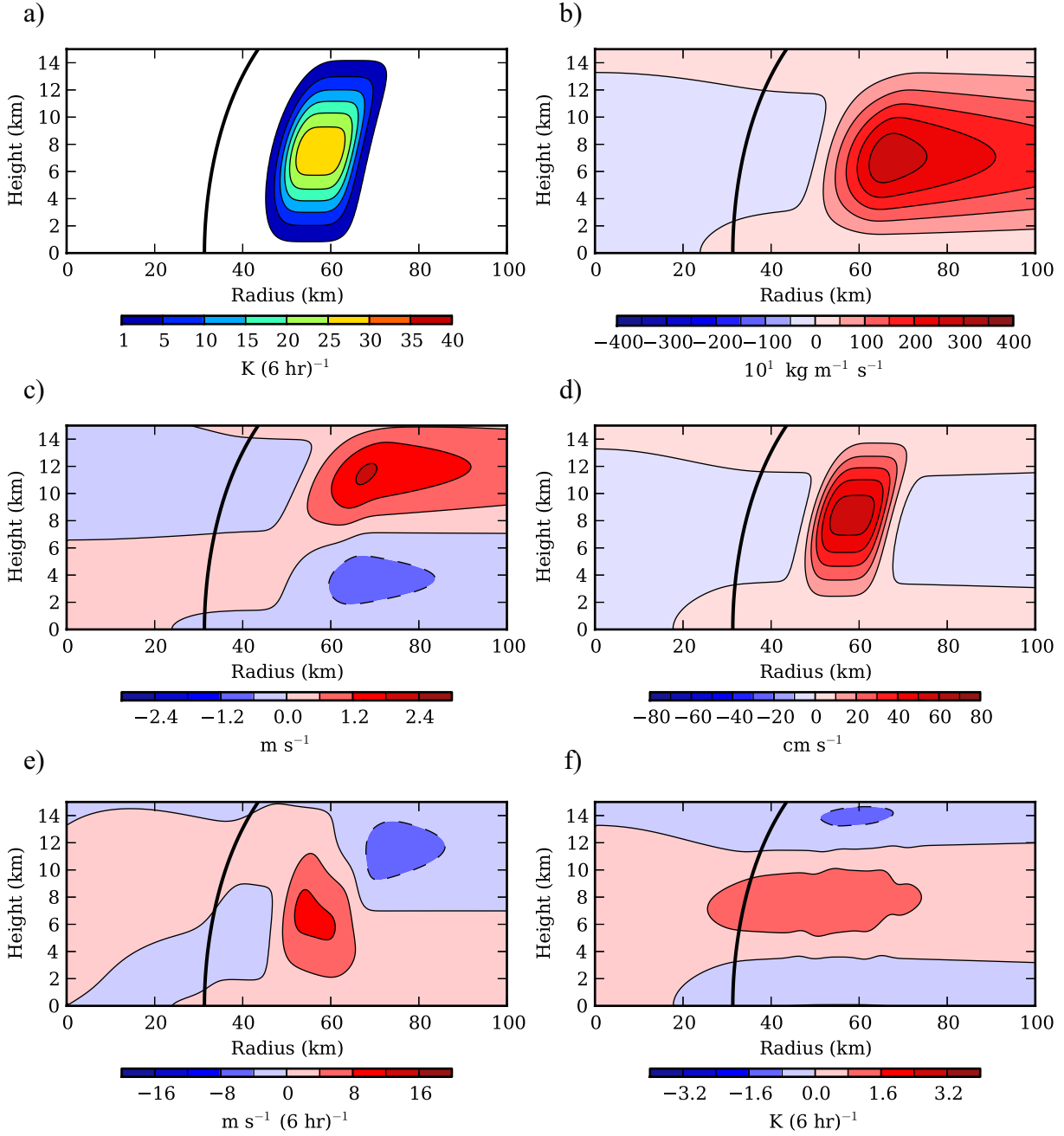
FIG. 2.13. Same as 2.12, except changes in vortex structure are for case H2.
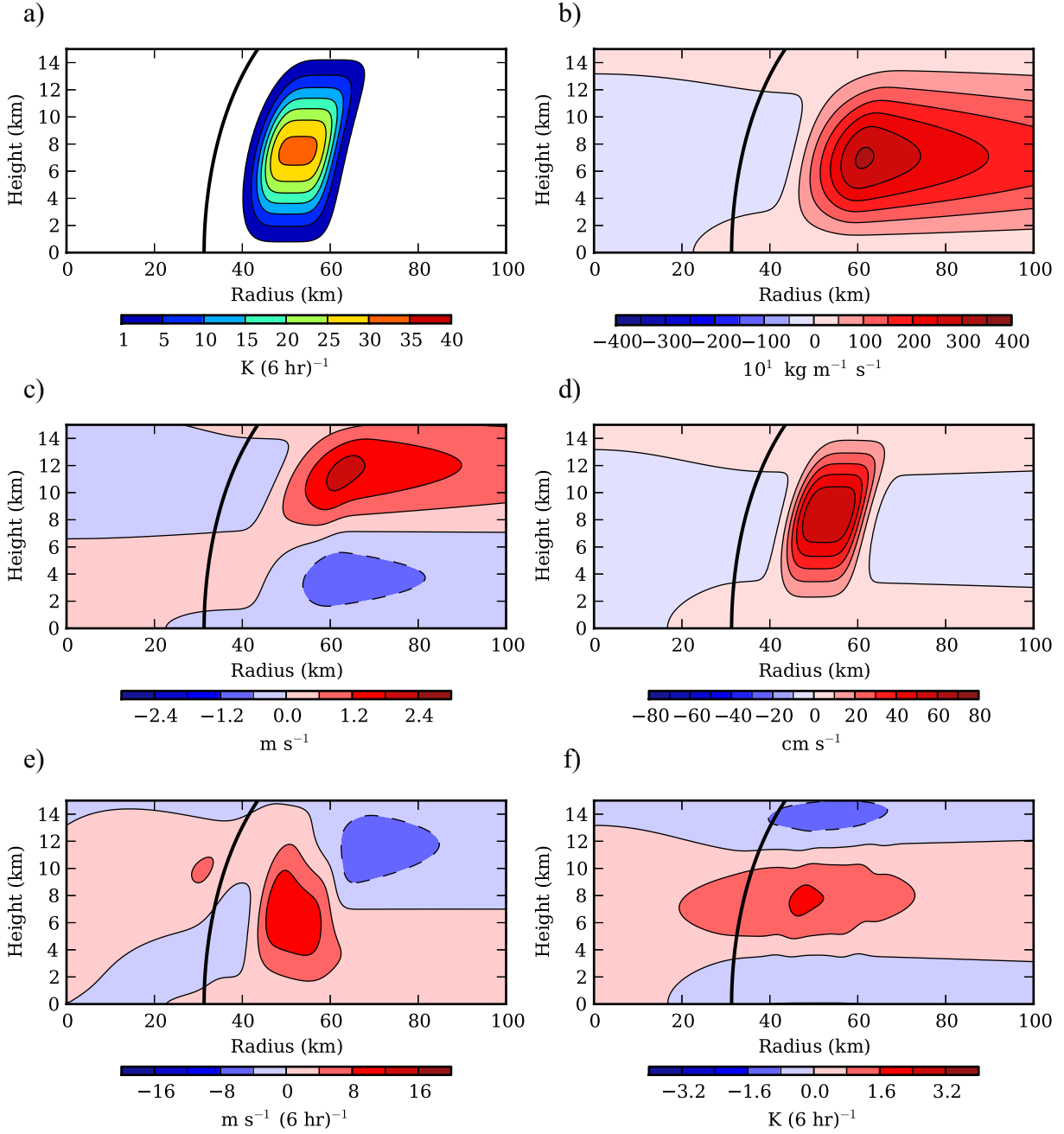
FIG. 2.14. Same as 2.12, except changes in vortex structure are for case H3.
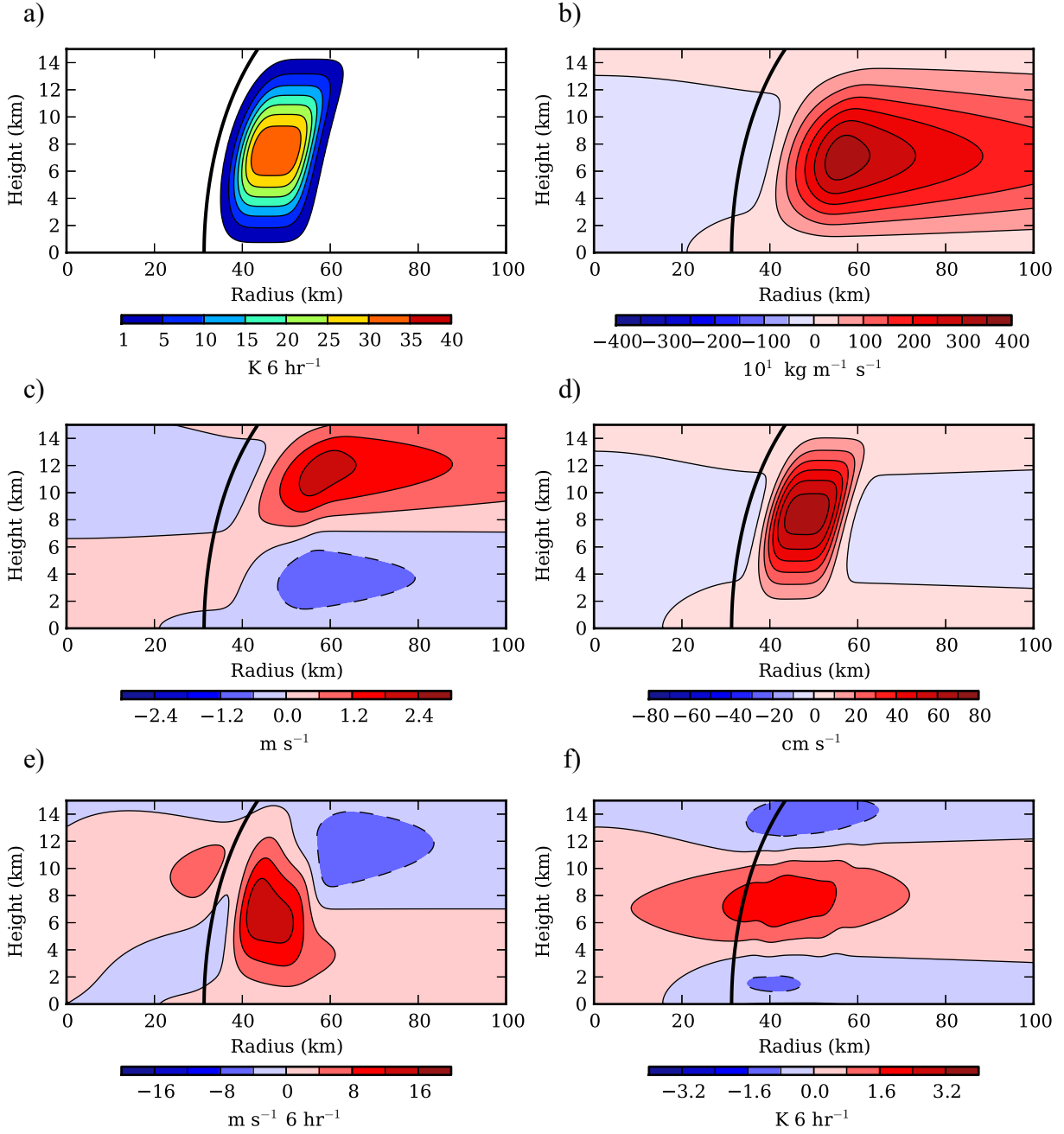
FIG. 2.15. Same as 2.12, except changes in vortex structure are for case H4.
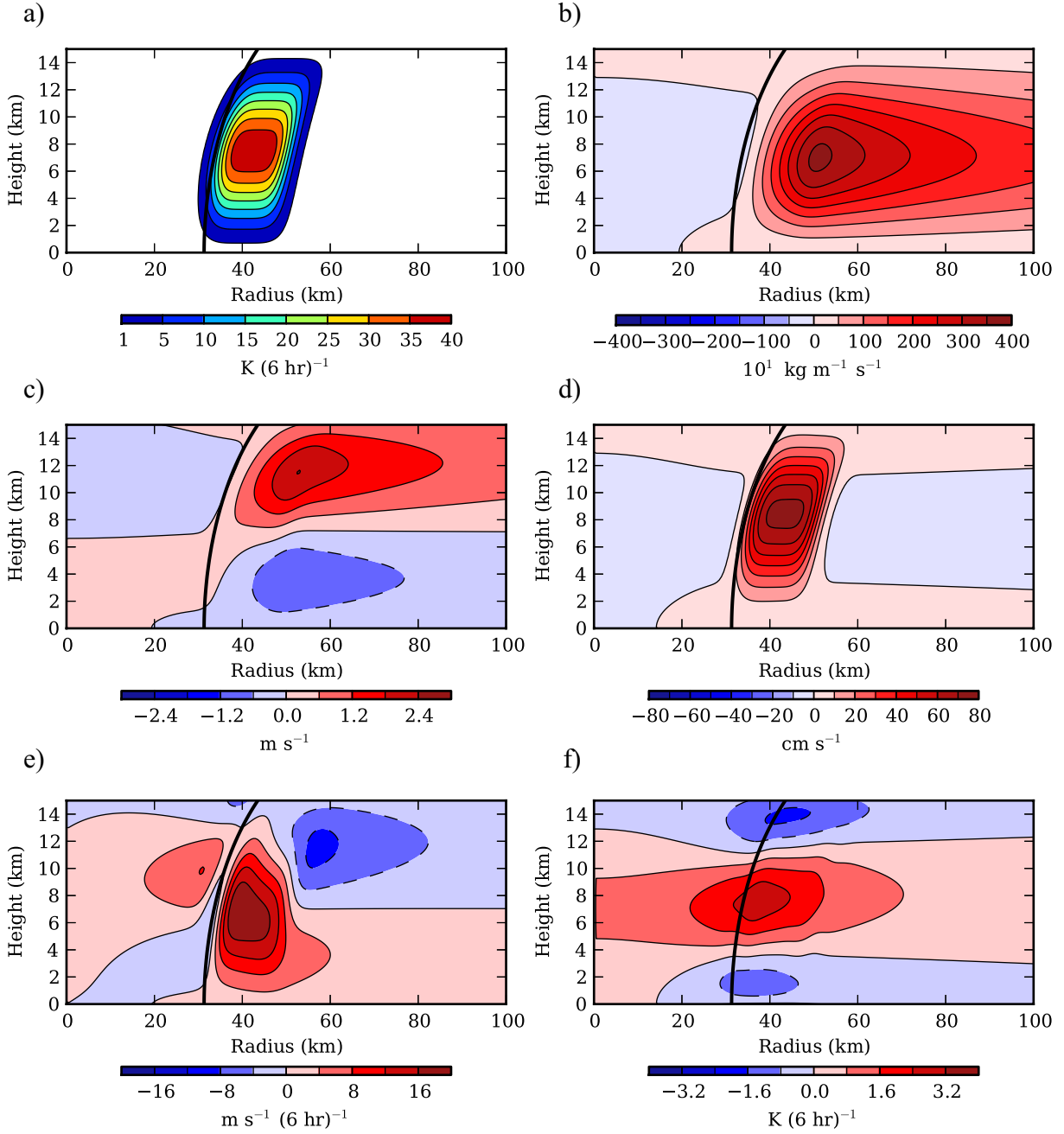
FIG. 2.16. Same as 2.12, except changes in vortex structure are for case H5.
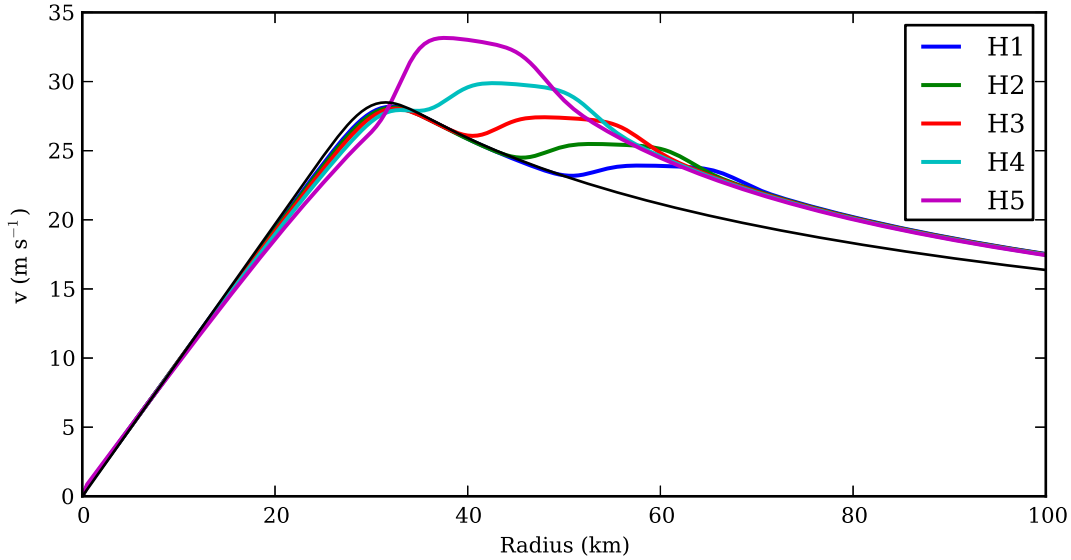
FIG. 2.17. The final tangential velocity at $z = 2$ km after applying the diabatic forcing for 6 hr. The black curve is the initial tangential velocity profile. The magenta curve is case H1, the cyan curve is case H2, the red curve is case H3, the green curve is case H4, and the blue curve is case H5.

2.6. DISCUSSION

The results from section 2.5 show the applications of the geopotential tendency and transverse circulation equations provide general concepts that can be applied to forecasting observed storms. The one-dimensional solver based on Musgrave et al. (2012) is applied to observed tropical cyclones. However, the limitations of the one-dimensional solutions are apparent. The one-dimensional solutions lack the ability to dissipate storms because of the exclusion of friction and boundary layer processes. In addition, the one-dimensional solutions have a constant static stability and zero baroclinicity. The two-dimensional solutions attempt to relax a few of the assumptions to improve the performance. The results show differences in the response to the diabatic forcing. The tendencies do not become as unrealistic as those seen in the one-dimensional solutions as the heating nears the region of high inertial stability. While this is more realistic than the one-dimensional solutions, at z_{max} the maximum tangential velocity shifts to the region of maximum

33

diabatic heating for the two-dimensional solutions. For cases H1–H3, it is more likely that the heating would not shift the radius of maximum wind. The two-dimensional solutions also capture some other interesting structural features of the tropical cyclone. Figs. 2.12–2.16 show adiabatic cooling above and below the region of strong diabatic heating (lower right panels) due to air still moving upward outside the region of heating. Another prominent feature is the acceleration of the tangential flow, positive $(\partial v/\partial t)$, near the stratosphere (lower left panels). Cyclonic motion is typically observed near the center of a hurricane as the vortex extends into the stratosphere. However, in the results shown here, this region does not extend far past the upper troposphere.

The two-dimensional solutions should improve the ability to predict the response to diabatic heating. However, observationally based runs are not included here because several issues related to using the rainfall rates need addressing. Taking the microwave satellite rainfall rates and computing the diabatic heating along angular momentum surfaces are difficult without understanding the vertical structure of the tropical cyclone. Not only does determining the diabatic heating from the microwave satellite rainfall rates pose an issue for $B \neq 0$, but also the rainfall rates contain stratiform rain. When the stratiform rain is in the region of high inertial stability, the tangential velocity tendency response is too large to be realistic. However, the best method for separating the stratiform rainfall from the convective rainfall is not clear. Despite this limitation, the models still provide powerful insight into how tropical cyclones intensify and aid in quantifying how and when rapid intensification will occur.

CHAPTER 3

SHOCK-LIKE STRUCTURES IN THE TROPICAL CYCLONE BOUNDARY LAYER

3.1. INTRODUCTION

Emanuel (2004), Bryan and Rotunno (2009a,b), and Bryan (2012) have stated that the drag

coefficient and horizontal diffusion in the boundary layer of the tropical cyclone play crucial roles

in the potential intensity of tropical cyclones, especially strong storms (category 4–5). However,

these models are unable to produce sharp gradients in tangential and radial momentum fields.

Williams et al. (2013) examine discontinuities in the wind field associated with Hurricane Hugo

(1989) to further explain the results seen by previous work.

On 15 September 1989, the NOAA aircraft with designation N42RF made a radial penetration

at 434 m ASL into Hurricane Hugo at the location indicated by the cyan arrow seen in Fig. 3.1. The

red curves in Fig. 3.2 show the aircraft data from the 434 m ASL radial penetration. A complete

account of this flight is given in Marks et al. (2008) and Zhang et al. (2011). As noted by Williams

et al. (2013), during the aircraft's inbound flight, the tangential velocity dropped by 60 m s^{-1} from

$r = 10$ km to $r = 7$ km, the radial velocity changed from 25 m s^{-1} inward to 10 m s^{-1} outward, and

the strongest updraft exceeded 20 m s^{-1}. On the outbound flight, the extreme jumps in tangential,

radial, and vertical velocities were not observed at 2682 m.

Instead of attributing the extreme boundary layer velocity structure to moist convective dynam-

ics, Williams et al. (2013) present the possibility that the structures can be replicated by non-linear

effects that can be represented by a simple dry hurricane slab boundary layer model. They inter-

pret the curves as axisymmetric with the blue curves representing the gradient balanced flow above

the boundary layer and the red curves as the flow contained in the boundary layer. In comparing

the results produced by the primitive equation slab boundary layer model to the aircraft data from

Hurricane Hugo (1989), the authors state that a boundary layer "shock-like" structure develops as a result of the dry dynamics. A shock is a mathematical discontinuity that develops as a result of non-linear effects deforming a smooth initial condition. A more detailed explanation of shocks and shock formation is provided in appendix B.
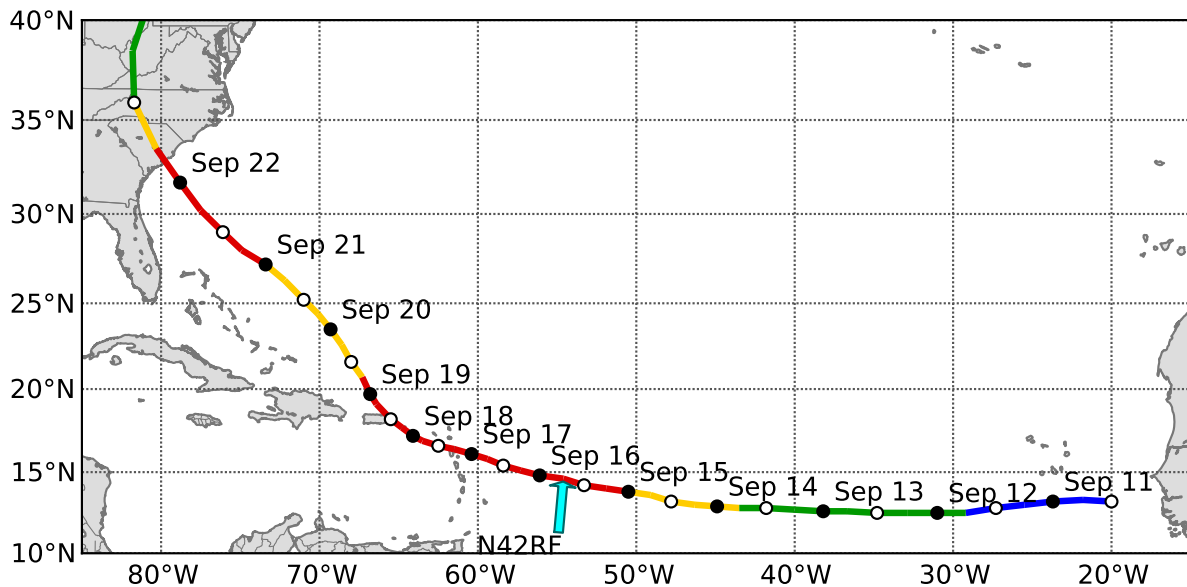
FIG. 3.1. National Hurricane Center track and intensity information for Hurricane Hugo (1989). The line depicts the track of the hurricane. The red line segments indicate where the storm is a major hurricane, category 3 and above; the yellow line segments indicate where the storm is a hurricane, category 1 and 2; the green line segments indicate tropical storm strength; the blue line segments indicate tropical depression. The dots indicate the time. Black dots represent the position at 00 UTC and are accompanied by a date label. White dots represent the position of the storm at 12 UTC. The cyan arrow represents the time and location for the radial penetration by the NOAA WP-3D (N42RF) aircraft.
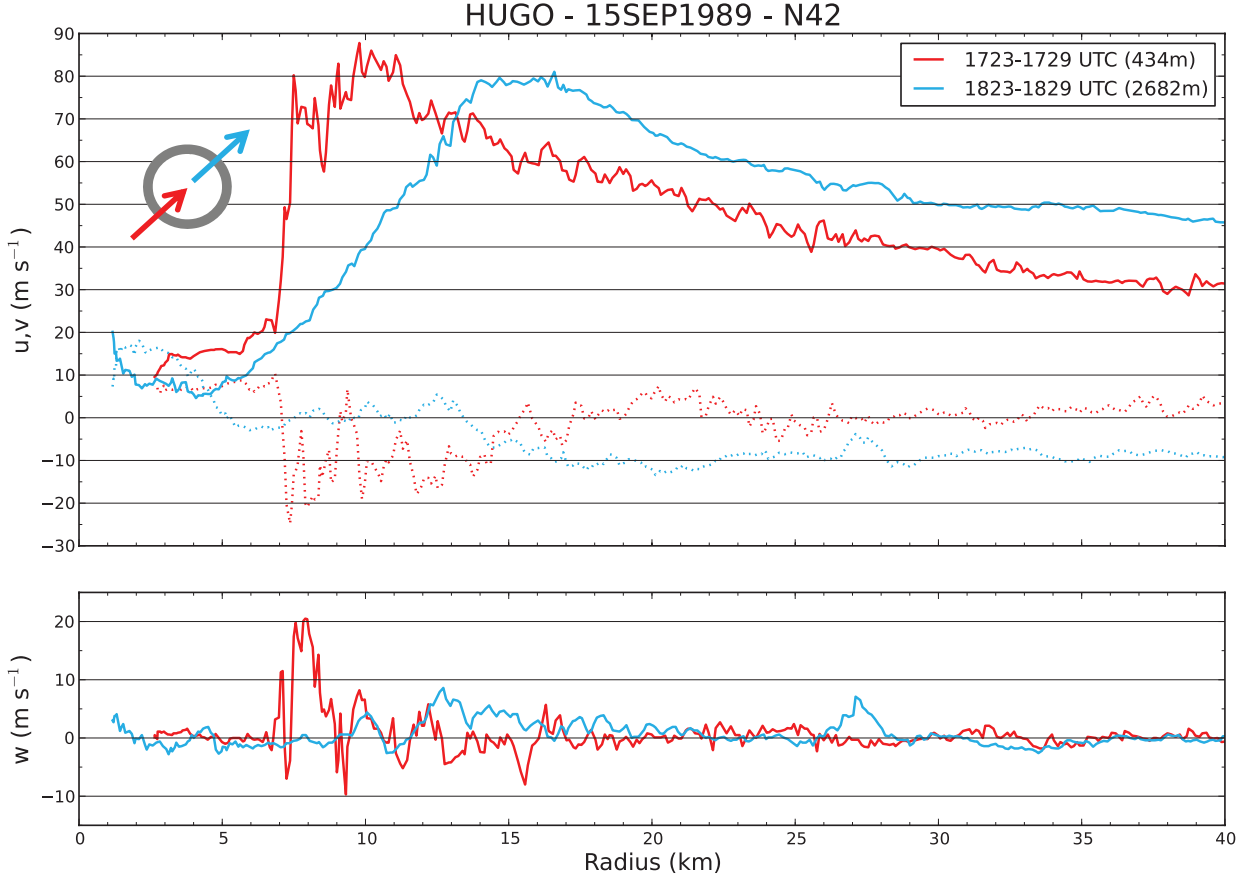
FIG. 3.2. NOAA WP-3D (N42RF) aircraft radial flight leg data for Hurricane Hugo on 15 September 1989. The red curves show the 434 m ASL inbound, southwest quadrant and the blue curves show the 2682 m ASL outbound, northeast quadrant. The solid curves in the upper panel show the tangential component of the wind and the dotted curves show the radial component of the wind. In the lower panel, the solid curves show the vertical component. The profiles are based on 1 second flight data and are in m s^{-1}.

3.2. PRIMITIVE EQUATION SLAB BOUNDARY LAYER MODEL

Williams et al. (2013) present a primitive equation slab boundary layer model that assumes axisymmetric motions of an incompressible fluid on an f-plane. The governing system of differential equations for the boundary layer variables of $u(r,t)$, $v(r,t)$, and $w(r,t)$ take the form

$$\frac{\partial u}{\partial t} = -u\frac{\partial u}{\partial r} - w^{-}\frac{u}{h} + \left(f + \frac{v + v_{\text{gr}}}{r}\right)(v - v_{\text{gr}}) - c_D U\frac{u}{h} + K\frac{\partial}{\partial r}\left(\frac{\partial(ru)}{r\partial r}\right), \qquad (3.1)$$

$$\frac{\partial v}{\partial t} = w^- \left(\frac{v_{\text{gr}} - v}{h} \right) - \left(f + \frac{\partial(rv)}{r\partial r} \right) u - c_D U \frac{v}{h} + K \frac{\partial}{\partial r} \left(\frac{\partial(rv)}{r\partial r} \right), \tag{3.2}$$

$$w = -h \frac{\partial(ru)}{r\partial r} \qquad \text{and} \qquad w^- = \frac{1}{2} \left(|w| - w \right), \tag{3.3}$$

where

$$U = 0.78 \left(u^2 + v^2 \right)^{\frac{1}{2}} \tag{3.4}$$

is the wind speed at 10 m height, f is the constant Coriolis parameter, and K is the constant horizontal diffusivity. Equation (3.4) comes from the analysis of dropwindsonde data by Powell et al. (2003). The drag coefficient, c_D, is assumed to depend on the wind speed U through the formula

$$c_D = 10^{-3} \begin{cases} 2.70/U + 0.142 + 0.0764\,U & \text{if } U \leq 25\,\text{m}\,\text{s}^{-1} \\[2mm] 2.16 + 0.5406 \left\{ 1 - \exp\left[-\frac{(U-25)}{7.5} \right] \right\} & \text{if } U \geq 25\,\text{m}\,\text{s}^{-1}. \end{cases} \tag{3.5}$$

Equation (3.5) is used by Williams et al. (2013) (see their Fig. 2 and corresponding text). The boundary conditions for (3.1) and (3.2) are

$$\left. \begin{aligned} u &= 0 \\[4mm] v &= 0 \end{aligned} \right\} \qquad \text{at} \quad r = 0, \tag{3.6}$$

$$\left. \begin{aligned} \frac{\partial(ru)}{\partial r} &= 0 \\[3mm] \frac{\partial(rv)}{\partial r} &= 0 \end{aligned} \right\} \qquad \text{at} \quad r = b, \tag{3.7}$$

where b is the radius of the outer boundary. The initial conditions are

$$u(r, 0) = u_0(r) \quad \text{and} \quad v(r, 0) = v_0(r), \tag{3.8}$$

where $u_0(r)$ and $v_0(r)$ are specified functions.

To understand further the numerical solutions presented by Williams et al. (2013) and extensions of this work to concentric eyewalls, it is useful to understand the formation of shocks through examining the characteristic form of the hyperbolic system. The following models present the solutions of (3.1)–(3.8) in a simple characteristic form. These analytical models aid in understanding the formation of the discontinuities in the radial and tangential flows within the boundary layer and the resulting singularities in vertical velocity and vorticity.

The two analytical models which are expressed by (3.9)–(3.10) and (3.38)–(3.39) differ from (3.1) and (3.2) that are used in the numerical results presented by Williams et al. (2013) because the numerical results begin with $u_0(r) = 0$. In the numerical results, u develops due to the forcing induced by the sub- and super-gradient flow $(v - v_{\mathrm{gr}})$, seen in the fourth term of (3.1). In the analytical solutions presented in this section, the shock develops as a result of the radial velocity having a nonzero initial condition and not the forcing.

3.3.1. ANALYTICAL MODEL I

Shocks form in the u and v fields in the hurricane boundary layer due to the $u(\partial u/\partial r)$ and $u[f + (\partial v/\partial r) + (v/r)]$ terms in equations (3.1) and (3.2). The $(v - v_{\mathrm{gr}})$ serves as the forcing mechanism for $(\partial u/\partial t)$. The frictional terms serve to damp u and v and the diffusion terms control the structure near the shock. To understand shock formation, we make the following approximations to (3.1) and (3.2). We neglect the horizontal diffusion terms, w^- terms, the surface drag terms, and the $(v - v_{\mathrm{gr}})$ forcing term. The equations simplify to

$$\frac{\partial u}{\partial t} + u\frac{\partial u}{\partial r} = 0, \tag{3.9}$$

39

$$\frac{\partial v}{\partial t} + u\left(f + \frac{\partial v}{\partial r} + \frac{v}{r}\right) = 0. \tag{3.10}$$

We can write equations (3.9) and (3.10) in the following form

$$\frac{du}{dt} = 0, \tag{3.11}$$

$$\frac{d\left(rv + \frac{1}{2}fr^2\right)}{dt} = 0, \tag{3.12}$$

where $(d/dt) = (\partial/\partial t) + u(\partial/\partial r)$. Integration of equations (3.11) and (3.12) using the initial conditions given in (3.8) results in the following solutions

$$u(r, t) = u_0(\hat{r}), \tag{3.13}$$

$$rv(r, t) = \hat{r}v_0(\hat{r}) + \frac{1}{2}f(\hat{r}^2 - r^2), \tag{3.14}$$

where the characteristics $\hat{r}(r, t)$ are given implicitly by

$$r = \hat{r} + tu_0(\hat{r}). \tag{3.15}$$

Equation (3.15) can be obtained through integrating $u(r, t)$ where $dr/dt = u$. For a given $\hat{r}$ in equation (3.15), a characteristic is defined in (r, t). Along this characteristic, this value of $u(r, t)$ is fixed, as shown by (3.13).

Unlike the system of equations for the slab boundary layer model presented at the beginning of section 3.2, Analytical Model I allows us to develop an equation for the time of shock formation and the radius of shock formation. To derive these equations, we must first understand where the

derivatives $(\partial u/\partial r)$ and $(\partial v/\partial r)$ become infinite. Taking $(\partial/\partial t)$ and $(\partial/\partial r)$ of (3.15) results in

$$-\frac{\partial \hat{r}}{\partial t} = \frac{u_0(\hat{r})}{1 + tu_0'(\hat{r})},$$
$$\frac{\partial \hat{r}}{\partial r} = \frac{1}{1 + tu_0'(\hat{r})}, \tag{3.16}$$

which means that $(\partial/\partial t)$ and $u(\partial/\partial r)$ of (3.13) are

$$\frac{\partial u}{\partial t} = u_0'(\hat{r})\frac{\partial \hat{r}}{\partial t} = -\frac{u_0(\hat{r})u_0'(\hat{r})}{1 + tu_0'(\hat{r})},$$
$$u\frac{\partial u}{\partial r} = u_0(\hat{r})u_0'(\hat{r})\frac{\partial \hat{r}}{\partial r} = \frac{u_0(\hat{r})u_0'(\hat{r})}{1 + tu_0'(\hat{r})}, \tag{3.17}$$

where u_0' is the derivative of the initial radial velocity profile, u_0. Equation (3.17) shows that (3.13) and (3.15) constitute a solution of (3.9). The same procedure can be used to show that (3.14) and (3.15) constitute a solution of (3.10). The solutions of (3.9) and (3.10) become multivalued. Because of this, a shock-capturing or -tracking procedure is required after the time of shock formation, t_s. To compute t_s for Analytical Model I, we use the denominators found on the right-hand side of (3.17) to show that the derivatives $(\partial u/\partial t)$ and $(\partial u/\partial r)$ become infinite when

$$tu_0'(\hat{r}) = -1. \tag{3.18}$$

Equation (3.18) shows the relationship between time and a specific characteristic curve defined by $\hat{r}$. If we denote $\hat{r}_s$ as the characteristic that corresponds to the minimum value of $u_0'(\hat{r})$, we can rewrite (3.18) to define the time of shock formation by setting $\hat{r} = \hat{r}_s$, which yields

$$t_s = -\frac{1}{u'(\hat{r}_s)}, \tag{3.19}$$

and the radius of shock formation as

$$r_s = \hat{r}_s - \frac{u_0(\hat{r}_s)}{u_0'(\hat{r}_s)}. \tag{3.20}$$

From the solutions (3.13) and (3.14), we can compute the relative vorticity and divergence. For relative vorticity, we differentiate (3.14), which yields

$$\zeta(r,t) = \frac{[f + \zeta_0(\hat{r})](\hat{r}/r)}{1 + tu_0'(\hat{r})} - f. \tag{3.21}$$

Likewise, differentiating (3.13) yields the following for the divergence

$$\delta(r,t) = \frac{u_0'(\hat{r})}{1 + tu_0'(\hat{r})} + \frac{u_0'}{r}. \tag{3.22}$$

Using the divergence, we can define the boundary layer pumping as $w(r,t) = -h\delta(r,t)$, which yields

$$w(r,t) = -h\left(\frac{u_0'(\hat{r})}{1 + tu_0'(\hat{r})} + \frac{u_0'}{r}\right). \tag{3.23}$$

From (3.21)–(3.23), we can see that the denominators contain the factor $[1 + tu_0'(\hat{r})]$. This implies that the relative vorticity, divergence, and boundary layer pumping become infinite at the same time and location.

To analyze the above equation, we consider the following initial conditions

$$u_0(r) = u_m\left(\frac{(n+1)(r/a)^n}{1 + n(r/a)^{n+1}}\right), \tag{3.24}$$

$$v_0(r) = v_m\left(\frac{(n+1)(r/a)^n}{1 + n(r/a)^{n+1}}\right), \tag{3.25}$$

where the constants a, n, u_m, and v_m specify the radial extent, shape parameter, and strength of the initial radial and tangential flow. For the results shown here, $n = 3$ in (3.24) and $n = 1$ in (3.25). The initial conditions for (3.24) and (3.25) are shown in Fig. 3.3 in a dimensionless form.
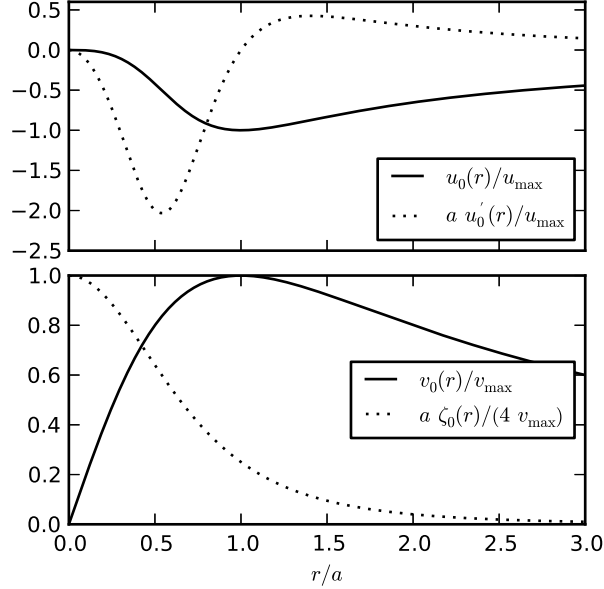
FIG. 3.3. The two panels depict the initial conditions for Analytical Model I in a dimensionless form. The top panel shows the dimensionless radial velocity computed from (3.24) in the solid line and the first derivative of the radial velocity computed from (3.26) in the dashed line. $n = 3$ for (3.24) and (3.26). The bottom panel shows the dimensionless tangential velocity profile computed from (3.25) in the solid line and the relative vorticity computed from (3.27) in the dashed line. $n = 1$ for (3.25) and (3.27).

From (3.24), we can define the derivative of the initial radial flow as

$$u_0'(r) = \frac{u_m}{a} \left(\frac{n(n+1)(r/a)^{n-1} \left[1 - (r/a)^{n+1}\right]}{\left[1 + n(r/a)^{n+1}\right]^2} \right), \tag{3.26}$$

and through (3.25), we obtain the initial relative vorticity

$$\zeta_0(r) = \frac{v_m}{a} \left(\frac{(n+1)^2 (r/a)^{n-1}}{\left[1 + n(r/a)^{n+1}\right]^2} \right). \tag{3.27}$$

43

Recall that the radius and time of shock formation are based on the minimum value of $u_0'(\hat{r})$. In the general case, the time of shock formation for Analytical Model I is

$$t_s = -\frac{1}{[u_0'(\hat{r})]_{\min}}. \tag{3.28}$$

In the case where n in the initial radial velocity profile, (3.24), is 3, we find that (3.20) is

$$\hat{r}_s = \left(2 - \frac{\sqrt{33}}{3}\right)^{1/4} a \approx 0.5402a \tag{3.29}$$

so that, from (3.26),

$$u_0'(\hat{r}_s) \approx 2.032\frac{u_m}{a}. \tag{3.30}$$

From (3.19), the time of shock formation can now be defined as

$$t_s \approx -\frac{a}{2.032u_m} \tag{3.31}$$

and the radius of shock formation as

$$r_s \approx 0.5426\,\hat{r}_s \approx 0.2931\,a. \tag{3.32}$$

The last two columns of Table 3.1 list the values of t_s and r_s for seven different vortex strengths given in the first column and the values of a, u_m, and v_m. Note that the values of t_s and r_s are only valid for the example where n is 3 for the radial flow, (3.24). For hurricane strength vortices (tropical cyclones with maximum velocities greater than or equal to 32 m s^{-1}), the time of shock formation is generally less than 1 hour. With these rapid shock formation times for strong vortices, it is possible that if the hurricane eyewall is disrupted, the hurricane eyewall can rapidly recover.

TABLE 3.1. The surface wind speed U, the radius of maximum inflow a, the maximum inflow velocity u_m, the maximum tangential velocity v_m, the shock formation time t_s, and the radius of shock formation r_s for seven selected vortices. The values of t_s and r_s have been computed from (3.31) and (3.32).

U (m s^{-1})	a (km)	u_m (m s^{-1})	v_m (m s^{-1})	t_s (hours)	r_s (km)
2.5	300	0.5	3.2	82.0	87.9
5	200	1.0	6.3	27.3	58.6
10	150	2.0	12.7	10.2	44.0
20	100	4.0	25.3	3.42	29.3
30	60	6.0	38.0	1.37	17.6
40	40	8.0	50.7	0.68	11.7
50	30	10.0	63.3	0.41	8.79

Staying with the initial conditions, (3.24) and (3.25) where n equals 3 and 1 respectively, the solutions (3.13) and (3.14) take the form

$$u(r,t) = u_m \left(\frac{4(\hat{r}/a)^3}{1 + 3(\hat{r}/a)^4} \right), \tag{3.33}$$

$$rv(r,t) = \hat{r} v_m \left(\frac{2(\hat{r}/a)}{1 + (\hat{r}/a)^2} \right) + \frac{1}{2} f(\hat{r}^2 - r^2), \tag{3.34}$$

where the characteristic curves are defined by

$$r = \hat{r} + u_m t \left(\frac{4(\hat{r}/a)^3}{1 + 3(\hat{r}/a)^4} \right). \tag{3.35}$$

From (3.21), the relative vorticity becomes

$$\zeta(r,t) = \left(f + \frac{4v_m}{a\left[1 + (\hat{r}/a)^2\right]^2} \right) \left(\frac{(\hat{r}/r)}{1 + tu_0'(\hat{r})} \right) - f, \tag{3.36}$$

while, through (3.23), the boundary layer pumping takes the form

$$w(r,t) = \left(\frac{4hu_m(\hat{r}/a)^2}{a[1 + 3(\hat{r}/a)^4]} \right) \left(\frac{3[1 - (\hat{r}/a)^4]}{[1 + tu_0'(\hat{r})][1 + 3(\hat{r}/a)^4]} + \frac{\hat{r}}{r} \right). \tag{3.37}$$

45

The solutions (3.33)–(3.35) are plotted in the two panels of Fig. 3.4 for the particular initial conditions given in the fifth line of Table 3.1. The plots cover the radial interval $0 \leq r \leq 100$ km and the time interval $0 \leq t \leq t_s$, where $t_s = 1.37$ hr is the shock formation time for this particular initial condition. Fig. 3.5 provides another view of the analytical solution for this model. In the figure, four panels display the radial profiles of u, v, w, and ζ where $t = 0$ hr is shown in blue and $t = 1.37$ hr is shown in red. Also shown in Fig. 3.5 are fluid particle displacements, black curves, for particles that are equally spaced at the initial time. At $t = t_s$, the u and v fields become discontinuous at $r = 17.6$ km, while the w and ζ fields become singular.
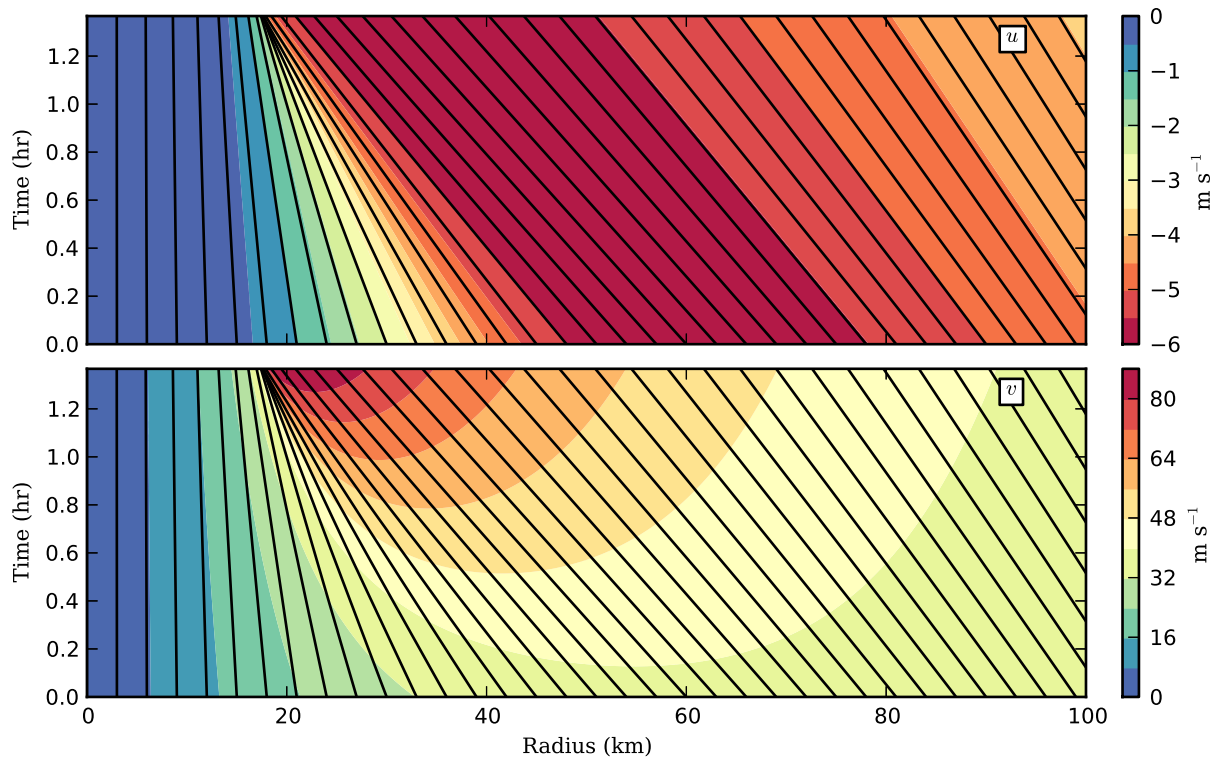
FIG. 3.4. The two panels show the analytical solutions for $u(r, t)$ and $v(r, t)$, as well as the characteristic curves, in the single eyewall case. These solutions are for the initial conditions (3.24) and (3.25) with the parameters from $U = 30$ m s^{-1} found in Table 3.1. The plots cover the time interval $0 \leq t \leq t_s$, where $t_s = 1.37$ hr is the shock formation time for this specific case.
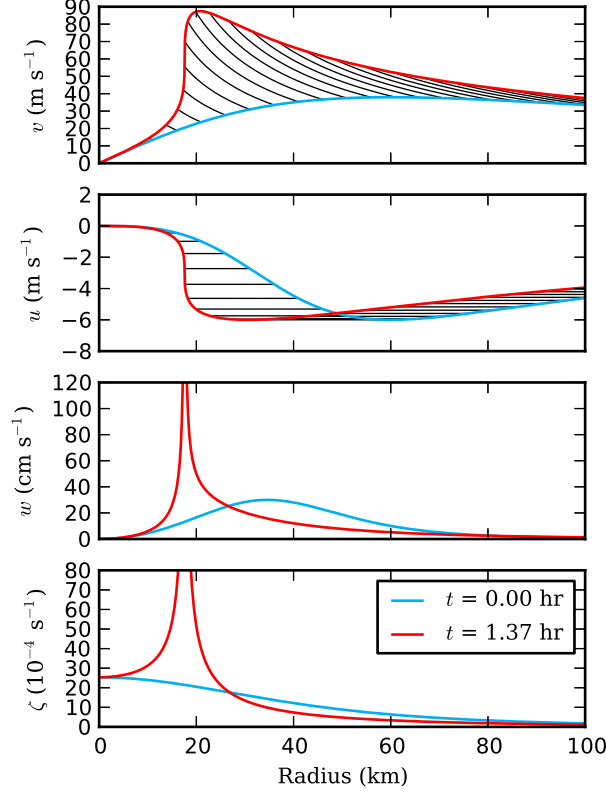
FIG. 3.5. The four panels display the radial profiles of u, v, w, ζ respectively at $t = 0$ (blue) and $t = t_s = 1.37$ hr (red). In the u and v panels, black curves show fluid particle displacements for particles that are equally spaced at the initial time. At $t = t_s$, the u and v fields become discontinuous at $r = 17.6$ km, while the w and ζ fields become singular at $r = 17.6$ km.

3.3.2. ANALYTICAL MODEL II

We now consider a second analytical model that adds surface drag effects. Linearizing the surface drag terms in (3.1) and (3.2), the radial and tangential momentum equations, (3.9) and (3.10), become

$$\frac{\partial u}{\partial t} + u\frac{\partial u}{\partial r} = -\frac{u}{\tau}, \tag{3.38}$$

$$\frac{\partial v}{\partial t} + u\left(f + \frac{\partial v}{\partial r} + \frac{v}{r}\right) = -\frac{v}{\tau}, \tag{3.39}$$

where $\tau = h/(c_D U)$ is the constant damping time scale. Some typical values of τ are given in Table 3.2 in the third column. These values are computed using a constant depth, $h = 1000$ m.

TABLE 3.2. The surface wind speed U, the drag coefficient times U, the character-istic damping time $\tau = h/(c_D U)$, the radius of maximum inflow a, the maximum inflow velocity u_m, the maximum tangential velocity v_m, and the shock formation time t_s for seven selected vortices. The values of t_s are computed from (3.54). r_s is not included in this table. As discussed in the text for (3.55), the values of r_s for Analytical Model I and Analytical Model II are equivalent.

U (m s^{-1})	$c_D U$ (cm s^{-1})	τ (hours)	a (km)	u_m (m s^{-1})	v_m (m s^{-1})	t_s (hours)
2.5	0.353	78.6	300	0.5	3.2	No Shock
5	0.532	52.2	200	1.0	6.3	38.7
10	1.18	23.6	150	2.0	12.7	13.4
20	3.61	7.69	100	4.0	25.3	4.52
30	7.27	3.82	60	6.0	38.0	1.69
40	10.51	2.64	40	8.0	50.7	0.791
50	13.41	2.07	30	10.0	63.3	0.457

The solutions to (3.38) and (3.39) can be obtained through writing them in the following form

$$\frac{d}{dt}\left(ue^{t/\tau}\right) = 0, \tag{3.40}$$

$$\frac{d}{dt}\left(rve^{t/\tau}\right) = -frue^{t/\tau}. \tag{3.41}$$

Through integration and use of the initial conditions, the solutions are

$$u(r,t) = u_0(\hat{r})e^{-t/\tau}, \tag{3.42}$$

$$rv(r,t) = \left\{\hat{r}v_0(\hat{r}) - f\left[\hat{r}t + u_0(\hat{r})\tau(t-\hat{t})\right]u_0(\hat{r})\right\}e^{-t/\tau}, \tag{3.43}$$

where the characteristics $\hat{r}(r,t)$ are given implicitly by

$$r = \hat{r} + \hat{t}u_0(\hat{r}), \tag{3.44}$$

where $\hat{t}$ is defined by

$$\hat{t} = \tau\left(1 - e^{-t/\tau}\right). \tag{3.45}$$

48

For a given $\hat{r}$, (3.44) defines a curved characteristic in (r, t), along which $u(r, t)$ exponentially damps according to (3.42). $v(r, t)$ also varies along the characteristic but not in the same manner as $u(r, t)$. $v(r, t)$ varies according to the factor $(\hat{r}/r)e^{-t/\tau}$. Since $(\hat{r}/r)$ can increase faster than $e^{-t/\tau}$, v will increase along some characteristics.

As in section 3.3.1, we will check the validity of (3.42) and (3.43) prior to defining the time and radius of shock formation by using (3.44) in combination with equations (3.40) and (3.41). We can also represent the solution (3.43) by eliminating (3.44) to show that

$$rv(r, t) = \left\{ \hat{r}v_0(\hat{r}) + f\left[\hat{r}\frac{t}{\hat{t}} + (r - \hat{r})\frac{\tau(t - \hat{t})}{\hat{t}^2} \right](\hat{r} - r) \right\} e^{-t/\tau}. \tag{3.46}$$

Equation (3.46) is analogous to the frictionless angular momentum form (3.14) presented with Analytical Model I. When $(t/\tau) << 1$, we see that $(t/\hat{t}) \approx 1$ and $\tau(t - \hat{t})/\hat{t}^2 \approx 1/2$ which means that (3.46) reduces to (3.14). We see that the derivatives $(\partial/\partial t)$ and $(\partial/\partial r)$ of (3.44) yield

$$-\frac{\partial \hat{r}}{\partial t} = \frac{u_0(\hat{r})e^{-t/\tau}}{1 + \hat{t}u_0'(\hat{r})},$$

$$\frac{\partial \hat{r}}{\partial r} = \frac{1}{1 + \hat{t}u_0'(\hat{r})}. \tag{3.47}$$

Again, similar to the steps taken to go from (3.16) to (3.17), we take the $(\partial/\partial t + 1/\tau)$ and $(\partial/\partial r)$ of (3.42) to yield

$$\frac{\partial u}{\partial t} + \frac{u}{\tau} = e^{-t/\tau}u_0'(\hat{r})\frac{\partial \hat{r}}{\partial t} = -\frac{e^{-2t/\tau}u_0(\hat{r})u_0'(\hat{r})}{1 + \hat{t}u_0'(\hat{r})},$$

$$u\frac{\partial u}{\partial r} = e^{-2t/\tau}u_0(\hat{r})u_0'(\hat{r})\frac{\partial \hat{r}}{\partial r} = \frac{e^{-2t/\tau}u_0(\hat{r}u_0'(\hat{r})}{1 + \hat{t}u_0'(\hat{r})}. \tag{3.48}$$

To compute the time of shock formation, we can take the denominators on the right-hand side of (3.48) to show that the derivatives of $(\partial u/\partial t)$ and $(\partial u/\partial r)$ become infinite when

$$\hat{t} u_0'(\hat{r}) = -1 \tag{3.49}$$

along one or more of the characteristics. Note that (3.49) is nearly identical to (3.18) with the exception that t is replaced by $\hat{t}$. Unlike (3.18), $\hat{t}$ is restricted to the range $0 \leq \hat{t} < \tau$. This means that it is possible that $\hat{t}$ does not become large enough for a shock to form. More specifically, a shock can form if and only if $\tau[u_0'(\hat{r})]_{\min} < -1$. From this condition, if the initial radial velocity profile has a large enough slope, the solution will become multivalued. If we define $\hat{r}_s$ as the characteristic curve that the shock originates along as the location of $[u_0'(\hat{r})]_{\min}$, then we can define the time of shock formation, from equations (3.45) and (3.49), as

$$t_s = -\tau \ln\left(1 + \frac{1}{\tau u_0'(\hat{r}_s)}\right), \tag{3.50}$$

and the radius of shock formation, determined from (3.44) and (3.49), as

$$r_s = \hat{r}_s - \frac{u_0(\hat{r}_s)}{u_0'(\hat{r}_s)}. \tag{3.51}$$

In assessing equations (3.50) and (3.51), we see that t_s is dependent upon the damping time scale τ. However, r_s is independent of τ. In comparing Analytical Models I and II, the values of r_s will be the same for the two models, but the t_s will differ. For shocks in hurricanes, $u_0(\hat{r}_s) < 0$ and $u_0'(\hat{r}_s) < 0$; therefore, the shock forms inside $\hat{r}_s$.

From the solutions of u and v, we can compute the relative vorticity through differentiation to yield

$$\zeta(r,t) = \left(\frac{\hat{r}}{r} \frac{\partial \hat{r}}{\partial r} \right) e^{-t/\tau} \left\{ \zeta_0(\hat{r}) - f \left[t \delta_0(\hat{r}) + \frac{2\tau^2 u_0(\hat{r}) u_0'(\hat{r})}{\hat{r}} \left(e^{-t/\tau} - 1 + \frac{t}{\tau} \right) \right] \right\}, \quad (3.52)$$

where $\zeta_0(\hat{r})$ is the initial relative vorticity and $\delta_0(\hat{r})$ is the initial divergence. The boundary layer pumping is

$$w(r,t) = -he^{-t/\tau} \left(\frac{\partial \hat{r}}{\partial r} u_0'(\hat{r}) + \frac{u_0(\hat{r})}{r} \right). \quad (3.53)$$

As in Analytical Model I, we can see that the boundary layer pumping and the relative vorticity become infinite at the same time and location.

Using the initial conditions given in equations (3.24) and (3.25) with $n = 3$ and $n = 1$ respectively (this specific set of initial conditions is depicted in Fig. 3.3), we can show that (3.50) becomes

$$t_s \approx -\tau \ln \left(1 + \frac{a}{2.032 \tau u_m} \right) \quad (3.54)$$

and (3.51) becomes

$$r_s \approx 0.5426 \hat{r}_s \approx 0.2931 a. \quad (3.55)$$

Table 3.2 contains values of t_s and r_s for seven different vortex strengths given in the first column. Note that the last column in Table 3.2 is the same as Table 3.1 with the exception of $U = 2.5 \text{ m s}^{-1}$. The weakest vortex in Table 3.2 does not form a shock because the surface drag effects prevent the discontinuities in u and v from developing. A storm with the initial conditions given in equations (3.24) and (3.25) must have a U that exceeds 2.66 m s^{-1} assuming $a = 300$ km.

Fig. 3.6 shows contours of shock formation time. The ordinate is the boundary layer wind speed that can be used to determine the strength of the tropical cyclone, U. The abscissa is the

radial advection time which is defined by the radius of maximum wind, a, divided by the maximum radial velocity, u_m. More intense storms are located near the upper left corner of the plot, while weak tropical storms are in the lower right corner of the plot. The plot suggests that shocks will develop over long periods of time in tropical storms but as storms intensify, the shocks develop rapidly. However, the threshold for shock development is small based on the radial advection time associated with strong tropical cyclones. Unlike Analytical Model I, Analytical Model II seems to suggest that, while shocks develop rapidly in strong cyclones, it is possible the shock may never reform if disrupted because of the small threshold. This results in the decay of the eyewall when the radial advection time increases. Landfall is one possible example of a disruption, which would cause the shock to not develop.
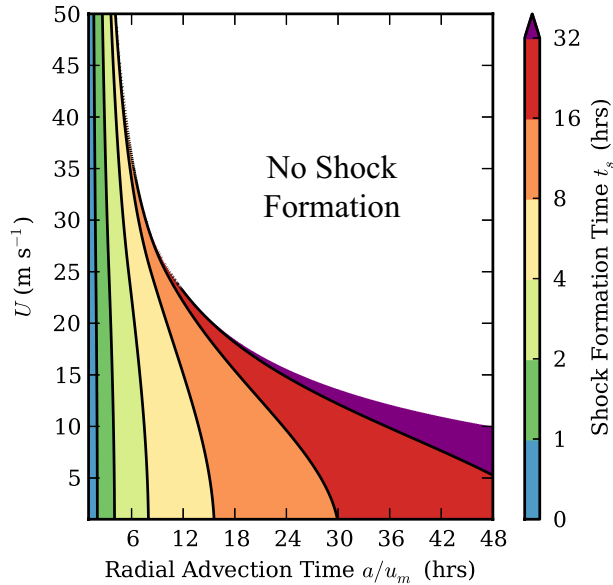
FIG. 3.6. The figure shows the analytical solutions for t_s computed from (3.50), with the initial conditions given in equations (3.24) and (3.25), as a function of the wind speed at 10 m, U, and radial advection time, a/u_m. t_s is contoured in a non-uniform interval to highlight features at short shock formation times.

3.3.2.1. SINGLE EYEWALL CASE

We now assess Analytical Model II for a single eyewall case. For the given initial conditions in (3.24) and (3.25), (3.42) and (3.46) take the form

$$u(r,t) = u_m \left(\frac{4(\hat{r}/a)^3 e^{-t/\tau}}{1 + 3(\hat{r}/a)^4} \right), \tag{3.56}$$

$$v(r,t) = v_m \left(\frac{2(\hat{r}/a)(\hat{r}/r)e^{-t\tau}}{1 + (\hat{r}/a)^2} \right), \tag{3.57}$$

where characteristic curves are defined by

$$r = \hat{r} + u_m \hat{t} \left(\frac{4(\hat{r}/a)^3}{1 + 3(\hat{r}/a)^4} \right). \tag{3.58}$$

Using (3.52), the relative vorticity takes the form

$$\zeta(r,t) = \left(\frac{4v_m}{a[1 + (\hat{r}/a)^2]^2} \right) \left(\frac{(\hat{r}/r)e^{-t\tau}}{1 + \hat{t}u_0'(\hat{r})} \right), \tag{3.59}$$

while, using (3.53), the boundary layer pumping takes the form

$$w(r,t) = \left(\frac{4hu_m e^{-t/\tau}(\hat{r}/a)^2}{a[1 + 3(\hat{r}/a)^4]} \right) \left(\frac{3[1 - (\hat{r}/a)^4]}{[1 + \hat{t}u_0'(\hat{r})][1 + 3(\hat{r}/a)^4]} + \frac{\hat{r}}{r} \right). \tag{3.60}$$

The solutions for $u(r,t)$, $v(r,t)$, $\hat{r}(r,t)$, as given by (3.56), (3.57), and (3.58), are plotted in the two panels of Fig. 3.7 for the particular initial condition given in the fifth row in Table 3.2. The plot covers the radial interval $0 \leq r \leq 100$ km and the time interval $0 \leq t \leq t_s$, where $t_s = 1.69$ hr is the shock formation time for this particular initial condition.
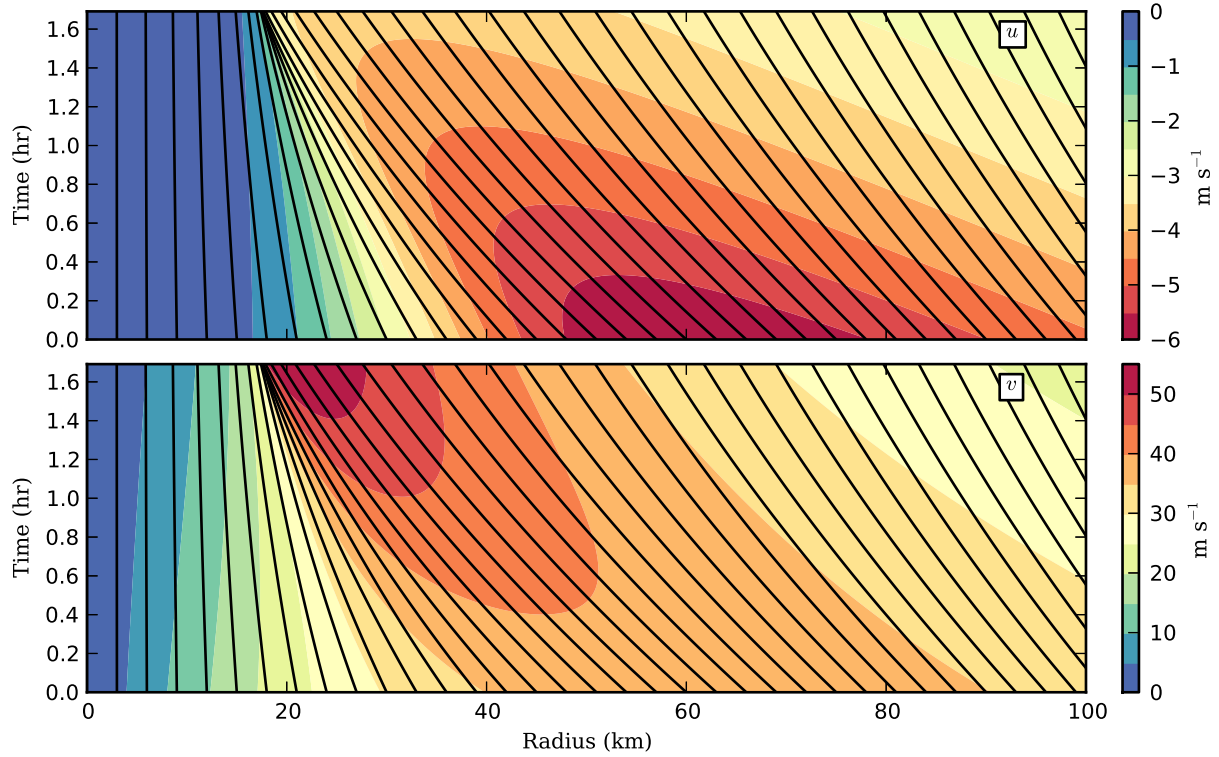
FIG. 3.7. The two panels show the analytical solutions for $u(r,t)$ and $v(r,t)$, as well as the characteristic curves, in the single eyewall case. These solutions are for the initial conditions (3.24) and (3.25) with the parameters from $U = 30$ m s^{-1} found in Table 3.2. The plots cover the time interval $0 \le t \le t_s$, where $t_s = 1.69$ hr is the shock formation time for this specific case.

Another view of this analytical solution is given in Fig. 3.8, with the four panels displaying the radial profiles (at $t = 0$ in blue and at $t = t_s$ in red) of u, v, w, ζ. Also shown by the black curves in the top two panels are fluid particle displacements for particles that are equally spaced at the initial time. At $t = t_s$, the u and v fields become discontinuous at $r = 17.6$ km, while the w and ζ fields become singular at $r = 17.6$ km.
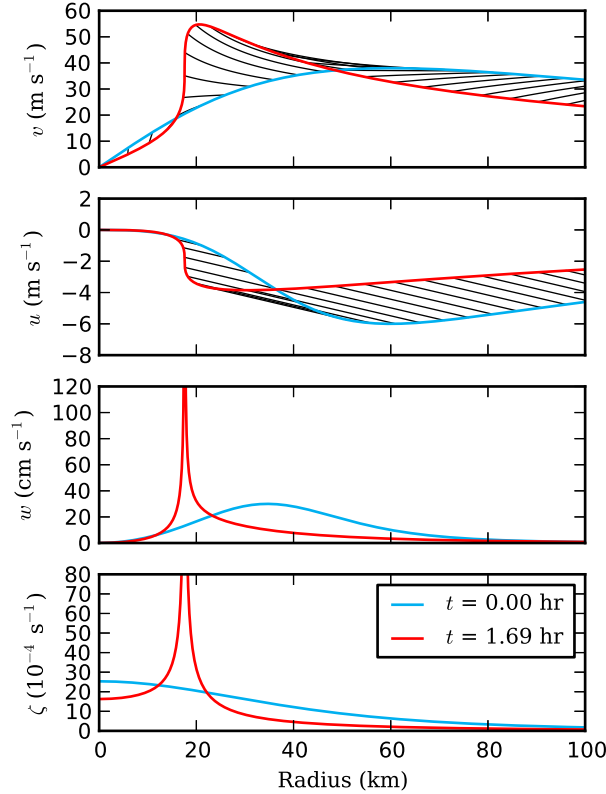
FIG. 3.8. The four panels display the radial profiles of u, v, w, ζ respectively at $t = 0$ (blue) and $t = t_s = 1.69$ hr (red). In the u and v panels, black curves show fluid particle displacements for particles that are equally spaced at the initial time. At $t = t_s$, the u and v fields become discontinuous at $r = 17.6$ km, while the w and ζ fields become singular at $r = 17.6$ km.

3.3.2.2. DOUBLE EYEWALL CASE

In recent years, there has been remarkable success in the numerical simulation of secondary eyewall formation and concentric eyewall cycles using three-dimensional models (Houze et al. 2007; Terwey and Montgomery 2008; Wang 2008a, 2009; Zhou and Wang 2009; Judt and Chen 2010; Abarca and Corbosiero 2011; Martinez et al. 2011; Rozoff et al. 2012; Wu et al. 2012; Huang et al. 2012; Menelaou et al. 2012; Lee and Chen 2012; Chen and Zhang 2013; Abarca and Montgomery 2013; Wang et al. 2013). These simulations, although run at larger horizontal grid spacing than the present axisymmetric slab model, can be interpreted as demonstrating the importance of the boundary layer shock phenomenon. One illuminating simulation by Rozoff et al.

(2012) shows that the destruction of the inner eyewall is closely associated with the development of a secondary eyewall shock at a larger radius (see their Fig. 2d). Simulations such as theirs are supportive of the notion that the fundamental interaction between concentric eyewalls occurs through the boundary layer and takes the form of a control and an ultimate destruction of the inner eyewall by the outer eyewall boundary layer shock.

In order to understand better the formation of concentric eyewalls, we now consider an example in which the initial condition leads to double shocks. In this second example, the initial radial and tangential winds are given by

$$u_0(r) = -\frac{4u_1(r/a_1)^3}{1 + 3(r/a_1)^4} - \frac{40u_2(r/a_2)^{39}}{1 + 39(r/a_2)^{40}}, \tag{3.61}$$

$$v_0(r) = \frac{2v_1(r/a_1)}{1 + (r/a_1)^2} + \frac{40v_2(r/a_2)^{39}}{1 + 39(r/a_2)^{40}}, \tag{3.62}$$

where the constants u_1, v_1, a_1, u_2, v_2, a_2 determine the strength and location of the initial inner and outer eyewall flows (shown in Fig. 3.9).
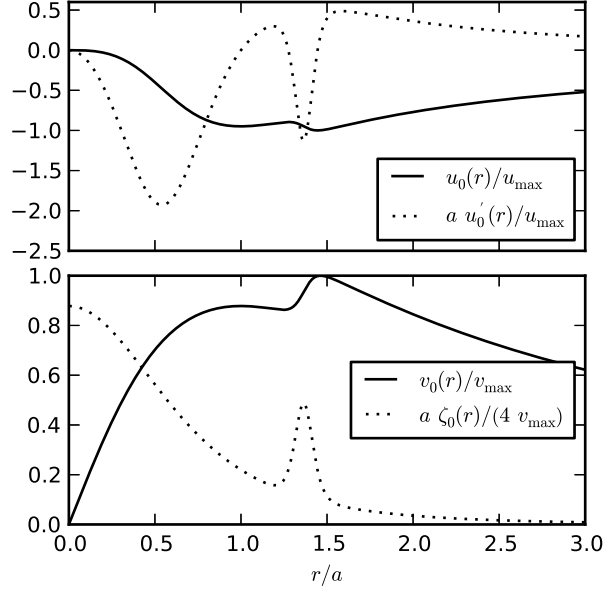
FIG. 3.9. The schematic shows two diagrams that depict the initial conditions for a double eyewall case in a dimensionless form. The top panel shows the dimensionless radial velocity computed from (3.61) as the solid line and the first derivative of the radial velocity computed from (3.63) in the dashed line. The bottom panel shows the dimensionless tangential velocity profile computed from (3.62) as the solid line and the relative vorticity computed from (3.64) in the dashed line.

The derivative of (3.40) is

$$u_0'(r) = -\frac{12u_1}{a_1}\left(\frac{(r/a_1)^2[1-(r/a_1)^4]}{[1+3(r/a_1)^4]^2}\right) - \frac{1560u_2}{a_2}\left(\frac{(r/a_2)^{38}[1-(r/a_2)^{40}]}{[1+39(r/a_2)^{40}]^2}\right), \qquad (3.63)$$

while, from differentiation of (3.41), the initial vorticity is

$$\zeta_0(r) = \frac{4v_1}{a_1[1+(r/a_1)^2]^2} + \frac{1600v_2(r/a_2)^{38}}{a_2[1+39(r/a_2)^{40}]^2}. \qquad (3.64)$$

This initial condition is similar to the single eyewall case except that there are secondary peaks

in the tangential and radial flows. We have chosen $u_1 = 6$ m s^{-1}, $v_1 = 38$ m s^{-1}, $a_1 = 60$ km,

$u_1 = 1.2$ m s^{-1}, $v_1 = 8$ m s^{-1}, $a_2 = 90$ km.

57

The analytical solutions for this double eyewall example are simply obtained through substituting (3.61)–(3.64) into (3.42)–(3.44) and (3.52)–(3.53). These solutions are shown in Figs. 3.10 and 3.11. As in the single eyewall case, an inner shock develops at $r = 17.6$ km and $t = 1.69$ hr. In addition, an outer shock has nearly developed by $t = 1.69$ hr. Because $u_0(\hat{r}_s)/u_0'(\hat{r}_s)$ is larger for the developing outer shock, the inward radial shift $(\hat{r}_s - r_s)$ predicted by (3.44) is larger for the developing outer shock, ≈ 31 km, than for the inner shock, ≈ 18 km.
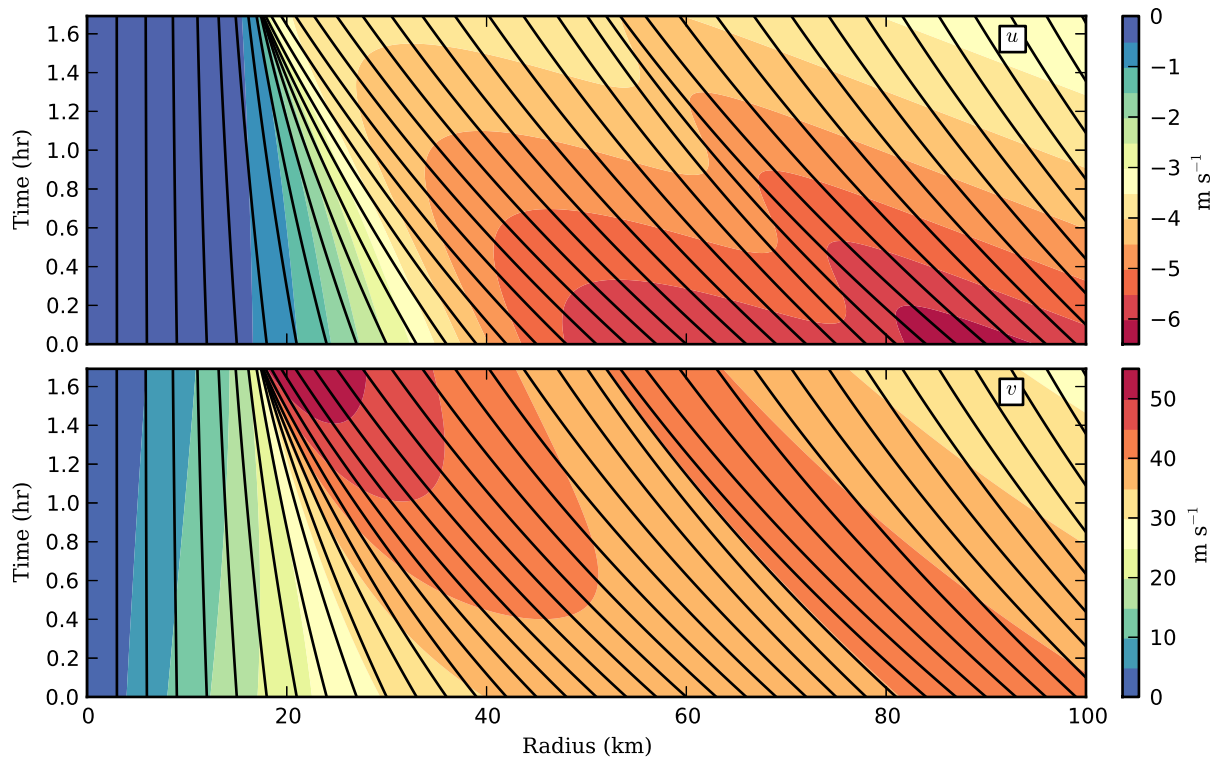
FIG. 3.10. The two panels show the analytical solutions for $u(r, t)$ and $v(r, t)$, as well as the characteristic curves, in the double eyewall case. These solutions are for the initial conditions (3.61) and (3.62) with the parameters from the text. The plots cover the time interval $0 \le t \le t_s$, where $t_s = 1.69$ hr is the shock formation time for this specific case.
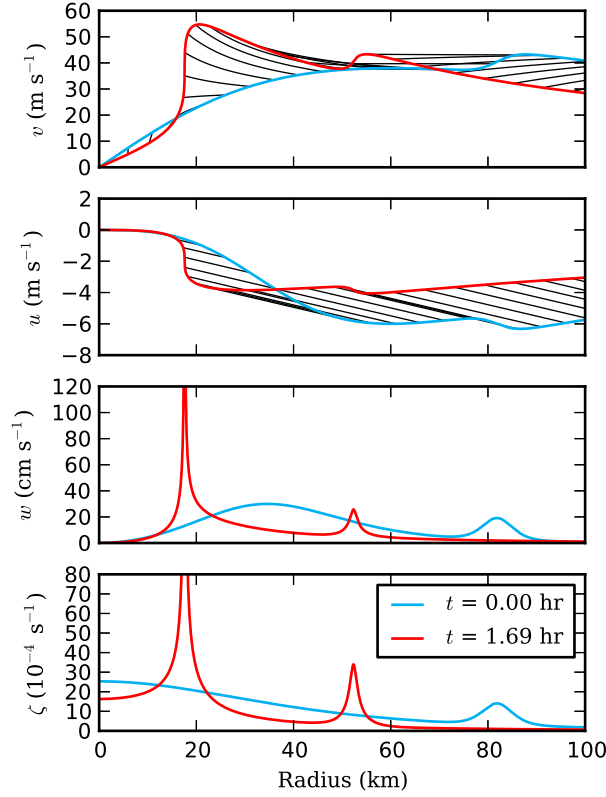
FIG. 3.11. The four panels display the radial profiles of u, v, w, ζ respectively at $t = 0$ (blue) and $t = t_s = 1.69$ hr (red). In the u and v panels, black curves show fluid particle displacements for particles that are equally spaced at the initial time. At $t = t_s$, the u and v fields become discontinuous at $r = 17.6$ km, while the w and ζ fields become singular $r = 17.6$ km.

3.4. DISCUSSION

The analytical results have a number of limitations. The primary limitation is that the results presented for both Analytical Model I and Analytical Model II are only plotted for the time interval $0 \leq t \leq t_s$. The solutions for both models become multivalued when the characteristics defined by (3.15) and (3.44) intersect. Williams et al. (2013) avoid this issue by using the equations for the slab boundary layer model presented at the beginning of section 3.2 and including horizontal diffusion. This could be applied to the analytical models developed here as well. However, a broad application of horizontal diffusion would result in solutions that are "shock-like" rather than a true mathematical shock. However, there are other methods to extend the solutions beyond $t = t_s$, into

the region of the (r, t)-plane where characteristics intersect and the solutions for $u(r, t)$, $v(r, t)$, and $\hat{r}(r, t)$ yield multivalued solutions. To exclude a broad application of horizontal diffusion and still maintain an analytical solution for the hurricane slab boundary layer, we can use the following procedure. Let $R(t)$ denote the shock at time t, where $t \geq t_s$. Let $\hat{r}_1(t)$ denote the label of the characteristic that just touches the inside edge of the shock at time t, and let $\hat{r}_2(t)$ denote the label of the characteristic that just touches the outside edge of the shock at time t. Then from (3.44), we obtain

$$R(t) = \hat{r}_1(t) + \tau \left(1 - e^{-t/\tau}\right) u_0(\hat{r}_1(t)), \tag{3.65}$$

$$R(t) = \hat{r}_2(t) + \tau \left(1 - e^{-t/\tau}\right) u_0(\hat{r}_2(t)), \tag{3.66}$$

which respectively determine $\hat{r}_1(t)$ and $\hat{r}_2(t)$ from a given $R(t)$. The last equation needed to track the shock is an appropriate jump condition across the shock, which yields a first order differential equation relating $dR(t)/dt$ to $\hat{r}_1(t)$ and $\hat{r}_2(t)$. This constitutes a shock-tracking procedure. Shock-capturing is a fundamental part of certain finite volume and finite difference methods based on the adaptive discretization concepts used in the essentially non-oscillatory (ENO) and the weighted essentially non-oscillatory (WENO) schemes (see the text by Durran (2010) and the review by Shu (1998)). ENO and WENO schemes add diffusion locally to the region around the shock. This differs from how diffusion is applied to the numerical model presented by Williams et al. (2013). Shock-capturing is also part of the finite volume methods used in the software package CLAW-PACK, described by LeVeque (2002). These capturing procedures are advantageous because they can reduce the smearing and nonphysical oscillations near the discontinuity.

The second limitation of the analytical models is that the radial equation of motion is unrealistic. The radial equation does not contain a source term proportional to $v - v_{gr}$. The result of this is that the radial inflow remains constant in Analytical Model I and damps in Analytical Model II.

This is a major difference between the results found in the numerical model presented by Williams et al. (2013) and the work here. This limitation cannot be corrected when using cylindrical coordinates. However, it is possible to create an analytical model using a system of equations for the boundary layer that is in Cartesian coordinates that would allow for a source term proportional to $v - v_{\mathrm{gr}}$ to be included.

The third limitation, only present in Analytical Model II, is the singularities that form in w and ζ. Such features are unrealistic in actual hurricanes. However, in a full-physics hurricane model, spikes in the boundary layer pumping are likely to be confined to an individual cumulonimbus cloud where the vertical velocity would be limited by the moist processes.

Despite the limitations of the analytical models, the analytical boundary layer models provide insight into what determines the size of the hurricane eye, how potential vorticity rings develop, how an outer concentric eyewall forms in addition to how it influences the inner eyewall, and why tropical cyclones are unable to fully recover after making landfall. The size of the hurricane eye is determined by the nonlinear processes that set the radius at which the eyewall shock forms and the location of the boundary layer pumping. As discussed with the models, the location of the pumping is also the location of the singularity in relative vorticity that shows where and how potential vorticity rings are produced. Through the pumping and latent heat release, the boundary layer potential vorticity ring is extended upward. In addition, the model provides insight into the works of Emanuel (2004), Bryan and Rotunno (2009a,b), and Bryan (2012). These studies discuss the importance of correctly parameterizing or modeling the drag coefficient and horizontal diffusion. However, this work shows that a more accurate approach to modeling strong tropical cyclones would be to resolve "shock-like" structures in the tropical cyclone boundary layer.

CHAPTER 4

CONCLUSIONS

In chapter 2, a one-dimensional elliptic solver, similar to the geopotential tendency equation solver developed by Musgrave et al. (2012), is applied to observed tropical cyclones. It is shown that while the one-dimensional solutions can predict the tangential velocity tendency response to diabatic forcing for some vortices, the one-dimensional solutions inadequately depict others. To address these inadequacies, two-dimensional solutions are developed to include baroclinicity. However, frictional influences are not incorporated into the solutions except through assuming the location of the vertical momentum flux out of the boundary layer and the implied location of the diabatic heating. The two-dimensional solutions produce a more realistic vertical structure and response to diabatic forcing when compared to the one-dimensional solutions. The two-dimensional solutions should provide more insightful information to use in improving statistical hurricane intensity predictions. Even with the improvements, the two-dimensional solutions still have limitations. Like the one-dimensional solutions, the two-dimensional solutions currently cannot dissipate the vortex unless some lower boundary layer conditions are set to allow for boundary layer frictional effects. Future work can assess improvements in using the two-dimensional solutions with observed vortices.

Chapter 3 explores "shock-like" structures in the tropical cyclone boundary layer. This chapter develops an analytical model to explain features observed in Hurricane Hugo (1989). Two models are presented in this section. The first lacks a damping force along the characteristics while the second includes damping. The models show that shocks develop in the tropical cyclone on rather short time scales. Analytical Model I indicates that if disrupted, the tropical cyclone will redevelop a shock quickly. Analytical Model II hints that it is possible for a tropical cyclone to be disrupted

and lack the ability to redevelop the shock. The shock determines the location of the boundary layer pumping which sets the location of the inner eyewall. In both models, the shock moves towards the center. This behavior is indicative of an eyewall contracting. With Analytical Model II, it is shown how a secondary shock would begin to develop. However, the influence of the secondary shock cannot be determined using the model in its current framework without implementing a shock-capturing or -fitting procedure, but the results do show why some storms develop while other dissipate due to wind speed and radial advection time. Future work can implement a shock-capturing or -fitting procedure to gain insight into shocks after the time of shock formation in an analytical framework to provide more insight into what types of dynamical conditions are required for tropical cyclone development. Also, future work could look at the squall line case to assess shock formation with the $(v - v_{\mathrm{gr}})$ forcing.

Chapters 2 and 3 are not completely unrelated. An extension for the work presented here offers one possible connection. If we look at Ooyama (1969a) and Ooyama (1969b), we can see how combining the two-dimensional solutions with a slab boundary layer model could provide crucial insight into the influence of shock-like structures on the life cycle of the tropical cyclone. Also, Fig. 1.3 shows how the location of the boundary layer pumping moves inward and the change to the tangential wind profile in both the boundary layer and the flow aloft. The two-dimensional successive over-relaxation technique could take the Ekman pumping from Williams et al. (2013) as the lower boundary condition and show how the gradient flow adjusts to the pumping.

REFERENCES

Abarca, S. F. and K. L. Corbosiero, 2011: Secondary eyewall formation in WRF simulations of Hurricane Rita and Katrina (2005). *Geophys. Res. Lett.*, **38**, L07 802.

Abarca, S. F. and M. T. Montgomery, 2013: Essential dynamics of secondary eyewall formation. *J. Atmos. Sci.*, **70**, submitted.

Bryan, G. H., 2012: Effects of surface exchange coefficients and turbulence length scales on the intensity and structure of numerically simulated hurricanes. *Mon. Wea. Rev.*, **140**, 1125–1143.

Bryan, G. H. and R. Rotunno, 2009a: Evaluation of an analytical model for the maximum intensity of tropical cyclones. *J. Atmos. Sci.*, **66**, 3042–3060.

Bryan, G. H. and R. Rotunno, 2009b: The maximum intensity of tropical cyclones in axisymmetric numerical model simulations. *Mon. Wea. Rev.*, **137**, 1770–1789.

Chen, H. and D.-L. Zhang, 2013: On the rapid intensification of Hurricane Wilma (2005), Part II: Convective bursts and upper-level warm core. *J. Atmos. Sci.*, **70**, 146–172.

Ciesielski, P. E., S. R. Fulton, and W. H. Schubert, 1986: Multigrid solution of an elliptic boundary value problem from tropical cyclone theory. *Mon. Wea. Rev.*, **114**, 797–807.

DeMaria, M. and J. D. Pickle, 1988: A simplified system of equations for simulation of tropical cyclones. *J. Atmos. Sci.*, **45**, 1542–1554.

DeMaria, M. and W. H. Schubert, 1985: Axisymmetric, primitive equation, spectral tropical cyclone model, Part II: Normal model initialization. *J. Atmos. Sci.*, **42**, 1225–1236.

Durran, D. R., 2010: *Numerical methods for fluid dynamics*. 2d ed., Springer, 504–523 pp.

Eliassen, A., 1951: Slow thermally or frictionally controlled meridional circulation in a circular vortex. *Astrophys. Norv.*, **5**, 19–60.

Eliassen, A., 1971: On the Ekman layer in a circular vortex. *J. Meteor. Soc. Japan*, **49**, 784–789.

Eliassen, A. and M. Lystad, 1977: The Ekman layer of a circular vortex – A numerical and theoretical study. *Geophys. Norv.*, **31**, 1–16.

Emanuel, K. A., 1997: Some aspects of hurricane inner-core dynamics and energetics. *J. Atmos. Sci.*, **54**, 1014–1026.

Emanuel, K. A., 2004: Tropical cyclone energetics and structure. *Atmospheric Turbulence and Mesoscale Meteorology*, E. Fedorovich, R. Rotunno, and B. Stevens, Eds., Cambridge University Press, 165–191.

Ferraro, R. R., 1997: SSM/I derived global rainfall estimates for climatological applications. *J. Geophys. Res.*, **102**, 16 715–16 735.

Ferraro, R. R., F. Weng, N. C. Grody, and L. Zhao, 2000: Precipitation characteristics over land from the NOAA-15 AMSU sensor. *Geophys. Res. Lett.*, **27**, 2669–2672.

Fudeyasu, H. and Y. Wang, 2011: Balanced contribution to the intensification of a tropical cyclone simulated with TCM4: Outercore spinup process. *J. Atmos. Sci.*, **68**, 430–449.

Fulton, S. R., 2011: A one-dimensional elliptic solver. Tech. rep., Department of Mathematics, Clarkson University, 9 pp., [Available upon request from the Schubert Research Group].

Fulton, S. R., P. E. Ciesielski, and W. H. Schubert, 1986: Multigrid methods for elliptic problems. *Mon. Wea. Rev.*, **114**, 943–959.

Fulton, S. R. and W. H. Schubert, 1985: Vertical normal mode transforms: Theory and applications. *Mon. Wea. Rev.*, **135**, 647–658.

Gopalakrishnan, S. and Coauthors, 2011: Hurricane Weather Research and Forecasting (HWRF) Model. Development Testbed Center, [Available online at http://www.emc.ncep.noaa.gov/HWRF/HWRFScientificDocumentation2011.pdf.].

Haltiner, G. J. and R. T. Williams, 1980: *Numerical prediction and dynamic meteorology*. 2d ed., John Wiley and Sons, Inc., 157-164 pp.

Houze, R. A., B. F. Chen, W.-C. Lee, and M. M. Bell, 2007: Hurricane intensity and eyewall replacement. *Science*, **315**, 1235–1239.

Huang, Y.-H., M. T. Montgomery, and C.-C. Wu, 2012: Concentric eyewall formation in Typhoon Sinlaku (2008). Part II: Axisymmetric dynamical processes. *J. Atmos. Sci.*, **69**, 662–674.

Judt, F. and S. S. Chen, 2010: Convectively generated potential vorticity in rainbands and formation of the secondary eyewall in Hurricane Rita of 2005. *J. Atmos. Sci.*, **67**, 3581–3599.

Kaplan, J., M. DeMaria, and J. A. Knaff, 2010: A revised tropical cyclone rapid intensification index for the Atlantic and eastern north Pacific basins. *Wea. Forecasting*, **25**, 220–241.

Kepert, J. D., 2010a: Slab- and height-resolving models of the tropical cyclone boundary layer. Part I: Comparing the simulations. *Quart. J. Roy. Meteor. Soc.*, **136**, 1686–1699.

Kepert, J. D., 2010b: Slab- and height-resolving models of the tropical cyclone boundary layer. Part II: Why the simulations differ. *Quart. J. Roy. Meteor. Soc.*, **136**, 1700–1711.

Knaff, J. A., M. DeMaria, D. A. Molenar, C. Sampson, and M. Seybold, 2011: An automated, objective, multi-satellite platform tropical cyclone surface wind analysis. *J. Appl. Meteor. Climatol.*, **50**, 2149–2166.

Lee, C.-Y. and S. S. Chen, 2012: Symmetric and asymmetric structures of hurricane boundary layer in coupled atmosphere-wave-ocean models and observations. *J. Atmos. Sci.*, **69**, 3576–3594.

LeVeque, R. J., 2002: *Finite volume methods for hyperbolic problems*. Cambridge University Press, 558 pp.

Lin, X. and R. H. Johnson, 1996: Kinematic and thermodynamic characteristics of the flow over the western Pacific warm pool during TOGA/COARE. *J. Atmos. Sci.*, **53**, 695–715.

Marks, F. D., P. G. Black, M. T. Montgomery, and R. W. Burpee, 2008: Structure of the eye and eyewall of Hurricane Hugo (1989). *Mon. Wea. Rev.*, **136**, 1237–1259.

Martinez, Y., G. Brunet, M. K. Yau, and X. Wang, 2011: On the dynamics of concentric eyewall genesis: Spacetime empirical normal modes diagnosis. *J. Atmos. Sci.*, **68**, 457–476.

Menelaou, K., M. K. Yau, and Y. Martinez, 2012: On the dynamics of the secondary eyewall genesis in Hurricane Wilma (2005). *Geophys. Res. Lett.*, **39**, L04 801.

Musgrave, K. D., R. K. Taft, J. L. Vigh, B. D. McNoldy, and W. H. Schubert, 2012: Time evolution of the intensity and size of tropical cyclones. *J. Adv. Model. Earth Syst.*, **4**, M08001.

Ooyama, K., 1969a: Numerical simulation of the life cycle of tropical cyclones. *J. Atmos. Sci.*, **26**, 3–40.

Ooyama, K., 1969b: Numerical simulation of tropical cyclones with an axi-symmetric model. *Proc. Third Symposium on Numerical Weather Prediction*, Tokyo, WMO/IUGG, 81–88.

Pendergrass, A. G. and H. E. Willoughby, 2009: Diabatically induced secondary flows in tropical cyclones. Part I: Quasi-steady forcing. *Mon. Wea. Rev.*, **137**, 805–821.

Powell, M. D., P. J. Vickery, and T. A. Reinhold, 2003: Reduced drag coefficient for high wind speeds in tropical cyclones. *Nature*, **422**, 279–283.

Rozoff, C. M., D. S. Nolan, J. P. Kossin, F. Zhang, and J. Fang, 2012: The roles of an expanding wind field and inertial stability in tropical cyclone secondary eyewall formation. *J. Atmos. Sci.*, **69**, 2621–2643.

Schubert, W. H. and M. DeMaria, 1985: Axisymmetric, primitive equation, spectral tropical cyclone model, Part I: Formulation. *J. Atmos. Sci.*, **42**, 1213–1224.

Shu, C.-W., 1998: Essentially non-oscillatory and weighted essentially non-oscillatory schemes for hyperbolic conservation laws. *Advanced numerical approximation of non-linear hyperbolic equations*, B. Cockburn, C. Johnson, C.-W. Shu, and E. Tadmor, Eds., Springer, No. 1697 in Lecture notes in mathematics, a. quarteroni ed., 325–432.

Slocum, C. J., 2012: Determining tropical cyclone intensity change through balanced vortex model applications. *Extended Abstracts, Thirtieth Conf. on Hurricanes and Tropical Meteorology*, Ponte Vedra Beach, FL, AMS.

Smith, R. K. and M. T. Montgomery, 2008: Balanced boundary layers in hurricane models. *Quart. J. Roy. Meteor. Soc.*, **134**, 1385–1395.

Smith, R. K. and S. Vogl, 2008: A simple model of the hurricane boundary layer revisited. *Quart. J. Roy. Meteor. Soc.*, **134**, 337–351.

Stoer, J. and R. Bulirsch, 1980: *Introduction to numerical analysis*. Springer-Verlag, 545–554 pp.

Terwey, W. D. and M. T. Montgomery, 2008: Secondary eyewall formation in two idealized, full-physics modeled hurricanes. *J. Geophys. Res.*, **113**, D12 112.

Toepfer, F., R. Gall, F. Marks, and E. Rappaport, 2010: Hurricane Forecast Improvement Program five year strategic plan. Tech. rep., HFIP Docs, 59 pp., [Available online at http://www.hfip.org/documents/].

Vigh, J. L. and W. H. Schubert, 2009: Rapid development of the tropical cyclone warm core. *J. Atmos. Sci.*, **66**, 3335–3350.

von Dommelen, L., 2011: Partial differential equations – The inviscid Burgers' equation. Tech. rep., Florida State University College of Engineering, 1 pp., [Available online at http://www.eng.fsu.edu/ dommelen/pdes/style_a/burgers.html].

Wang, X., Y. Ma, and N. E. Davidson, 2013: Secondary eyewall formation and eyewall replacement cycles in a simulated hurricane: Effect of the net radial force in the hurricane boundary layer. *J. Atmos. Sci.*, **70**, 1317–1341.

Wang, Y., 2008a: Rapid filamentation zone in a numerically simulated hurricane. *J. Atmos. Sci.*, **65**, 1158–1181.

Wang, Y., 2008b: Structure and formation of an annular hurricane simulated in a fully compressible, nonhydrostatic model – TCM4. *J. Atmos. Sci.*, **65**, 1505–1527.

Wang, Y., 2009: How do outer spiral rainbands affect tropical cyclone structure and intensity? *J. Atmos. Sci.*, **66**, 1250–1273.

Whitham, G. B., 1974: *Linear and nonlinear wave*. Wiley, 636 pp.

Williams, G. J., R. K. Taft, B. D. McNoldy, and W. H. Schubert, 2013: Shock-like structures in the tropical cyclone boundary layer. *J. Adv. Model. Earth Syst.*, **accepted**.

Willoughby, H. E., 1979: Forced secondary circulations in hurricanes. *J. Geophys. Res.*, **84**, 3173–3183.

Wu, C.-C., Y.-H. Huang, and G.-Y. Lien, 2012: Concentric eyewall formation in Typhoon Sinlaku (2008). Part I: Assimilation of t-parc data based on ensemble Kalman filer (EnKF). *Mon. Wea. Rev.*, **140**, 506–527.

Xu, J. and Y. Wang, 2010: Sensitivity of the simulated tropical cyclone inner core size and intensity of the radial distribution of surface entropy flux. *J. Atmos. Sci*, **67**, 1831–1852.

Yamasaki, M., 1977: The role of surface friction in tropical cyclones. *J. Meteor. Soc. Japan*, **55**, 559–571.

Yanai, M., S. Esbensen, and J.-H. Chu, 1973: Determination of bulk properties of tropical cloud clusters from large scale heat and moisture budgets. *J. Atmos. Sci.*, **30**, 611–627.

Zhang, J. A., F. D. Marks, M. T. Montgomery, and S. Lorsolo, 2011: An estimation of turbulent characteristics in the low-level region of Hurricanes Allen (1980) and Hugo (1989). *Mon. Wea. Rev.*, **139**, 1447–1462.

Zhou, X. and Y. Wang, 2009: From concentric eyewall to annular hurricane: A numerical study with the cloud resolved WRF model. *Geophys. Res. Lett.*, **36**, L03 802.

APPENDIX A

SOLUTIONS OF THE TRANSVERSE CIRCULATION EQUATION

A.1. NINE POINT LOCAL SMOOTHER

In section 2.5.2, a modified Rankine vortex, defined by equation (2.38), is used for the tangential velocity field. However, the tangential velocity profile is not smooth and the vorticity has a discontinuity at the radius of maximum wind. To avoid issues these aspects may cause, the velocity field is smoothed prior to calculating the static stability, baroclincity, and inertial stability and solving using an iterative method. The smoother applied to the tangential velocity field is a nine point local smoother.

$$
v(j,k)^{\text{smooth}} = \begin{cases}
\frac{1}{4}v_{j,k} + \frac{1}{8}\left(v_{j-1,k} + v_{j,k-1} + v_{j+1,k} + v_{j,k+1}\right) & \\
\quad + \frac{1}{16}\left(v_{j-1,k+1} + v_{j-1,k-1} + v_{j+1,k-1} + v_{j+1,k+1}\right) & \text{if } 0 < j < J \text{ and } 0 < k < K \\[2mm]
\frac{1}{3}v_{j,k} + \frac{1}{6}\left(v_{j-1,k} + v_{j,k-1} + v_{j,k+1}\right) & \\
\quad + \frac{1}{12}\left(v_{j-1,k+1} + v_{j-1,k-1}\right) & \text{if } j = J \text{ and } 0 < k < K \\[2mm]
\frac{1}{3}v_{j,k} + \frac{1}{6}\left(v_{j-1,k} + v_{j+1,k} + v_{j,k+1}\right) & \\
\quad + \frac{1}{12}\left(v_{j-1,k+1} + v_{j+1,k+1}\right) & \text{if } 0 < j < J \text{ and } k = 0 \\[2mm]
\frac{1}{3}v_{j,k} + \frac{1}{6}\left(v_{j-1,k} + v_{j,k-1} + v_{j+1,k}\right) & \\
\quad + \frac{1}{12}\left(v_{j-1,k-1} + v_{j+1,k-1}\right) & \text{if } 0 < j < J \text{ and } k = K \\[2mm]
\frac{4}{9}v_{j,k} + \frac{2}{9}\left(v_{j-1,k} + v_{j,k-1}\right) + \frac{1}{9}v_{j-1,k-1} & \text{if } j = J \text{ and } k = K \\[2mm]
\frac{4}{9}v_{j,k} + \frac{2}{9}\left(v_{j-1,k} + v_{j,k+1}\right) + \frac{1}{9}v_{j-1,k+1} & \text{if } j = J \text{ and } k = 0 \\[2mm]
v_{j,k} & \text{if } j = 0
\end{cases}
\tag{A.1}
$$

The result of applying the above filter to v multiple times is similar to a Gaussian convolution. In this work, we apply the nine point local smoother 100 times to v. This technique varies from a traditional nine point local smoother in that the outer boundaries are smoothed as well with one exception. The inner boundary remains constant as seen in the last line of (A.1). The inner boundary for v must remain zero.

A.2. LATERAL BOUNDARY CONDITION

Because the two-dimensional elliptic problem is being solved numerically on a finite domain, we would like to formulate a lateral boundary condition that results in a solution that is essentially the same as would be obtained on an infinite domain. The basic idea is that the forcing, through $Q(r, z)$ and/or $\psi_0(r)$, is confined to an inner region. Far outside this region the forcing vanishes, the static stability A becomes a function of z only, the baroclinicity B vanishes, and the inertial stability C becomes f^2/ρ, so that the partial differential equation (2.11) simplifies to

$$\frac{\partial}{\partial r}\left(\frac{\partial(r\psi)}{r\partial r}\right) + \frac{f^2}{N^2}e^{-z/H}\frac{\partial}{\partial z}\left(e^{z/H}\frac{\partial\psi}{\partial z}\right) = 0 \tag{A.2}$$

in the outer region, where we have defined the buoyancy frequency $N(z)$ by $N^2(z) = \rho A$. Assuming the solution of (A.2) has the separable form $\psi(r, z) = \Psi(r)\mathcal{Z}(z)$, the partial differential equation separates into the two ordinary differential equations

$$\frac{d}{dr}\left(\frac{d(r\Psi)}{r\,dr}\right) = \frac{f^2}{c^2}\Psi, \tag{A.3}$$

$$e^{-z/H}\frac{d}{dz}\left(e^{z/H}\frac{d\mathcal{Z}}{dz}\right) = -\frac{N^2}{c^2}\mathcal{Z}, \tag{A.4}$$

where $1/c^2$ is the separation constant. As discussed by Fulton and Schubert (1985), the vertical structure equation (A.4), with appropriate top and bottom boundary conditions, has a spectrum of

eigenvalues $c = c_0, c_1, c_2, \cdots c_n$. Using the mean tropical atmosphere profile for $N(z)$ and using

a lid at $z_T = 15$ km, typical values of c are $c_0 \approx 250$ m s^{-1} for the external mode, $c_1 \approx 50$ m s^{-1}

for the first internal mode, $c_2 \approx 25$ m s^{-1} for the second internal mode, etc. This means that the

horizontal structure equation (A.3) is to be solved for each vertical mode. Equation (A.3) can then

be written in the form

$$r^2 \frac{d^2 \Psi_m}{dr^2} + r \frac{d\Psi_m}{dr} - \left(\mu_m^2 r^2 + 1 \right) \Psi_m = 0, \tag{A.5}$$

where $\mu_m = f/c_m$ is the inverse of the Rossby length for the mth vertical mode. We can write

the general solution of (A.5) as a linear combination of the first-order modified Bessel functions

$I_1(\mu_m r)$ and $K_1(\mu_m r)$. Since $I_1(\mu_m r)$ rapidly grows with r, we set its coefficient to zero, so that

the solution of (A.5) becomes $\Psi_m(r) = \alpha_m K_1(\mu_m r)$. The constants α_m are unknown and depend

on the details of the forcing in the central region. However, these constants can be eliminated by

using the Bessel function derivative relation

$$\frac{d[r K_1(\mu_m r)]}{r \, dr} = -\mu_m K_0(\mu_m r)$$

to obtain

$$\frac{d\Psi_m}{dr} = -\frac{\Psi_m}{\ell_m} \quad \text{at} \quad r = r_B, \tag{A.6}$$

where

$$\frac{1}{\ell_m} = \frac{1}{r_B} + \frac{\mu_m K_0(\mu_m r_B)}{K_1(\mu_m r_B)}. \tag{A.7}$$

If only the first internal mode is involved, this translates to

$$\frac{\partial \psi}{\partial r} = -\frac{\psi}{\ell} \quad \text{at} \quad r = r_B. \tag{A.8}$$

Table A.1 contains values for ℓ based on r_B.

TABLE A.1. The table gives approximate values for ℓ used in the lateral boundary condition in (A.8). The values of ℓ were computed using (A.7) where $u_m \approx f/c_1$. c_1 is the first internal mode with a value of 50 m s^{-1}.

r_B (km)	ℓ (km)
600	441.8
900	558.5
1200	638.5
1500	695.7

For more detailed discussions of the lateral boundary condition, see Schubert and DeMaria (1985), DeMaria and Schubert (1985), and DeMaria and Pickle (1988).

A.3. NUMERICAL METHODS

The most efficient way to solve the two-dimensional elliptic problem (2.11) is via multigrid methods (e.g. see the review by Fulton et al. (1986) and the particular application by Ciesielski et al. (1986)). If efficiency is not an issue, a very simple successive over-relaxation procedure is adequate. Thus, we now solve a finite difference version of the transverse circulation problem using successive over-relaxation. To discretize (2.11), we use centered finite difference approximations on the grid points $(r_j, z_k) = (j\Delta r, k\Delta z)$ with $j = 0, 1, \ldots, J$ and $k = 0, 1, \ldots, K$, where $\Delta r = r_B/J$ and $\Delta z = z_T/K$. We solve the discrete equations using the following successive over-relaxation procedure. Denoting the current (i.e. iteration ν) solution estimate by $\psi_{j,k}^{(\nu)}$, and sweeping through the grid in lexicographic order, we first compute the current residual of (2.11) from

$$\mathcal{R}_{j,k} = \mathcal{D}_{j,k}^{(rr)} + \mathcal{D}_{j,k}^{(rz)} + \mathcal{D}_{j,k}^{(zr)} + \mathcal{D}_{j,k}^{(zz)} - F_{j,k}, \tag{A.9}$$

where

$$\mathcal{D}_{j,k}^{(rr)} = \frac{1}{(\Delta r)^2} \left\{ A_{j+\frac{1}{2},k} \left(a_{j+1} \psi_{j+1,k}^{(\nu)} - b_j \psi_{j,k}^{(\nu)} \right) - A_{j-\frac{1}{2},k} \left(a_j \psi_{j,k}^{(\nu)} - b_{j-1} \psi_{j-1,k}^{(\nu+1)} \right) \right\}, \quad \text{(A.10)}$$

$$\mathcal{D}_{j,k}^{(rz)} = \frac{1}{4(\Delta r)(\Delta z)} \left\{ B_{j+1,k} \left(\psi_{j+1,k+1}^{(\nu)} - \psi_{j+1,k-1}^{(\nu+1)} \right) - B_{j-1,k} \left(\psi_{j-1,k+1}^{(\nu)} - \psi_{j-1,k-1}^{(\nu+1)} \right) \right\}, \quad \text{(A.11)}$$

$$\mathcal{D}_{j,k}^{(zr)} = \frac{1}{4(\Delta r)(\Delta z)} \left\{ B_{j,k+1} \left(\psi_{j+1,k+1}^{(\nu)} - \psi_{j-1,k+1}^{(\nu)} + \frac{2\Delta r}{r_j} \psi_{j,k+1}^{(\nu)} \right) \right.$$
$$\left. - B_{j,k-1} \left(\psi_{j+1,k-1}^{(\nu+1)} - \psi_{j-1,k-1}^{(\nu+1)} + \frac{2\Delta r}{r_j} \psi_{j,k-1}^{(\nu+1)} \right) \right\}, \quad \text{(A.12)}$$

$$\mathcal{D}_{j,k}^{(zz)} = \frac{1}{(\Delta z)^2} \left\{ C_{j,k+\frac{1}{2}} \left(\psi_{j,k+1}^{(\nu)} - \psi_{j,k}^{(\nu)} \right) - C_{j,k-\frac{1}{2}} \left(\psi_{j,k}^{(\nu)} - \psi_{j,k-1}^{(\nu+1)} \right) \right\}, \quad \text{(A.13)}$$

$$F_{j,k} = \frac{g}{c_p T_0} \left(\frac{Q_{j+1,k} - Q_{j-1,k}}{2\Delta r} \right), \quad \text{(A.14)}$$

$$a_j = 1 + \frac{\Delta r}{2r_{j-\frac{1}{2}}} \quad \text{and} \quad b_j = 1 - \frac{\Delta r}{2r_{j+\frac{1}{2}}}. \quad \text{(A.15)}$$

The solution estimate $\psi_{j,k}^{(\nu)}$ is then updated by

$$\psi_{j,k}^{(\nu+1)} = \psi_{j,k}^{(\nu)} + \frac{\omega \mathcal{R}_{j,k}}{G_{j,k}}, \quad \text{(A.16)}$$

where ω is the over-relaxation factor and

$$G_{j,k} = \frac{a_j A_{j-\frac{1}{2},k} + b_j A_{j+\frac{1}{2},k}}{(\Delta r)^2} + \frac{C_{j,k-\frac{1}{2}} + C_{j,k+\frac{1}{2}}}{(\Delta z)^2}. \quad \text{(A.17)}$$

Equations (A.9)–(A.17) are computed at the grid points $1 \le j \le J - 1, \ 1 \le k \le K - 1$. Finally, the outer boundary points are updated from the outer boundary condition (A.8) written in the form

$$\psi_{J,k} = \left(1 - \frac{\Delta r}{\ell} \right) \psi_{J-1,k} \quad \text{for} \quad 1 \le k \le K - 1. \quad \text{(A.18)}$$

Equations (A.9)–(A.18) are iterated, starting with the initial estimate $\psi_{j,k}^{(1)} = 0$. This initial estimate does not change on the top, bottom, and inner boundaries. For the numerical solutions presented here, we have used the domain $0 \leq r \leq 1200$ km and $0 \leq z \leq 30$ km, and a grid with $J = 2400$ and $K = 300$, resulting in the grid spacing $\Delta r = 500$ m

Note from (A.10) and (A.13) that the discrete operator tends to be locally isotropic if $(\Delta r / \Delta z) \approx (N/\hat{f})$, where $N = (\rho A)^{1/2}$ is the buoyancy frequency and $\hat{f} = (\rho C)^{1/2}$ is the effective Coriolis parameter. Because $\hat{f}$ varies so much across the domain, it is not possible to maintain discrete local isotropy with fixed $(\Delta r / \Delta z) = 5$. Local isotropy does occur in regions where $\hat{f} \approx N/5 \approx 40f$. In the outer regions, $\hat{f}$ is much smaller than $40f$, so a larger Δr in the outer regions would be more isotropic in the local sense. In spite of the large spatial variation in $\hat{f}$, the successive over-relaxation procedure works well if care is taken to optimize the over-relaxation parameter ω.

Since the rate of convergence of the successive over-relaxation procedure is sensitive to the choice of the relaxation parameter ω, it is important to find the optimal value. In order to gauge the convergence rate, we have monitored the rate of decrease of the residual norm as iteration proceeds, where the residual norm is defined by

$$\text{Residual Norm} = \left(\sum_{j=1}^{J-1} \sum_{k=1}^{K-1} \mathcal{R}_{j,k}^2 \right)^{1/2}. \tag{A.19}$$

Although the transverse circulation problem (2.11) involves coefficients that can vary considerably in radius and height (especially the inertial stability C), we can use the simpler Poisson problem (i.e. $B = 0$, with A and C positive constants) as a guide for the optimal value of ω. In successive over-relaxation, the optimal value of ω lies between 1 and 2. In the case where $\omega = 1$, the iterative method reduces to Gauss-Seidel. Finding the optimal ω decreases the number of iterations required for the solution to converge. As discussed by Haltiner and Williams (1980), for the

Poisson problem with a grid of J points in the horizontal and K points in the vertical, the optimal value of ω for the Poisson problem is

$$\omega_{\text{optimal}}^{\text{Poisson}} \approx 2 - \pi\sqrt{2}\left(\frac{1}{J^2} + \frac{1}{K^2}\right)^{1/2} \approx 2 - \frac{\pi\sqrt{2}}{K} = 1.97, \quad\quad\quad (A.20)$$

where the second approximate equality follows from the assumption that $J \gg K$, as in our case with $J = 2400$ and $K = 300$.

Although this value of 1.97 is a useful rough guide, we have experimentally refined it and found that an over-relaxation factor of 1.99668 optimal for the cases investigated here (shown in Fig. A.1). Experience shows that, with this value of the over-relaxation factor ω, the residual norm (A.19) can be reduced by six or seven orders of magnitude in 5000 iterations, Fig. A.2, which is well beyond the accuracy required for present purposes.
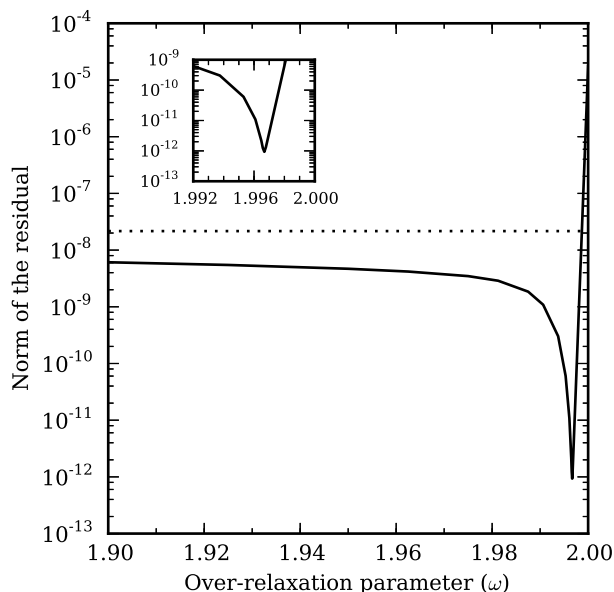
FIG. A.1. The plot shows the norm of the residual for $1.9 \leq \omega \leq 2.0$. Through experimentation, the optimal ω is 1.99668. The dashed line shows the norm of the residual for Gauss-Seidel, $\omega = 1$. The insert plot zooms in on the optimal value for ω.
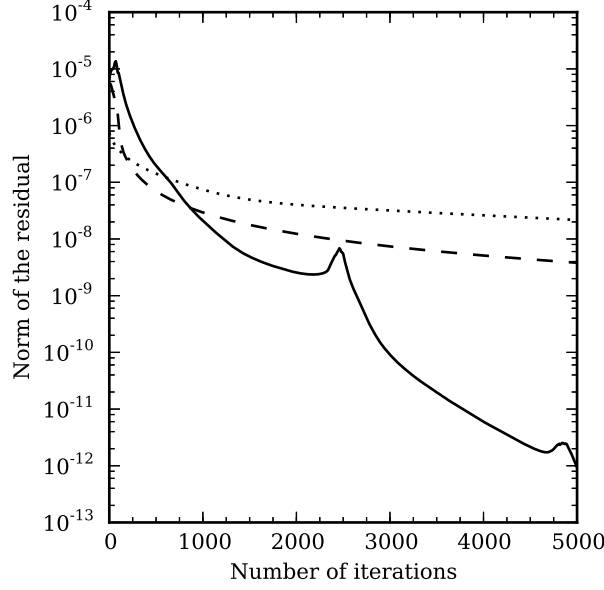
FIG. A.2. The plot shows the value of the norm of the residual for values of ω per iteration out to 5000 iterations. The optimal ω value, 1.99668, is in the solid curve. The dotted curve is for the Gauss-Seidel iterative method where $\omega = 1$ and the dashed curve used the optimal ω, 1.97, predicted by (A.20).

After convergence, we can compute the velocity components of the transverse circulation from

$$u_{j,k} = \frac{\psi_{j,k-1} - \psi_{j,k+1}}{2\rho_k \Delta z}, \tag{A.21}$$

$$w_{j,k} = \frac{\psi_{j+1,k} - \psi_{j-1,k}}{2\rho_k \Delta r} + \frac{\psi_{j,k}}{\rho_k r_j}, \tag{A.22}$$

and the temperature and tangential wind tendencies from

$$\left(\frac{\partial T}{\partial t}\right)_{j,k} = -u_{j,k}\left(\frac{\partial T}{\partial r}\right)_{j,k} - w_{j,k}\left(\frac{\partial T}{\partial z} + \frac{RT}{c_p H}\right)_{j,k} + \frac{Q_{j,k}}{c_p}, \tag{A.23}$$

$$\left(\frac{\partial v}{\partial t}\right)_{j,k} = -u_{j,k}\left(f + \frac{\partial(rv)}{r\partial r}\right)_{j,k} - w_{j,k}\left(\frac{\partial v}{\partial z}\right)_{j,k}. \tag{A.24}$$

76

APPENDIX B

SHOCKS

We begin with the advection equation

$$\frac{\partial q}{\partial t} + c\frac{\partial q}{\partial x} = 0, \tag{B.1}$$

where q is a quantity being advected by a wind c. When $c(\partial q/\partial x)$ is non-linear, the solution does not translate uniformly across the domain. For the non-linear case, the initial condition deforms with time and a shock, a discontinuous solution will develop. As discussed by LeVeque (2002), a fundamental feature of non-linear conservation laws is the spontaneous development of discontinuities originating from smooth initial conditions.

If we take (B.1) and replace q and c with the wind, u, we have the inviscid Burgers' equation,

$$\frac{\partial u}{\partial t} + u\frac{\partial u}{\partial x} = 0. \tag{B.2}$$

To illustrate that u does not translate uniformly across the domain, we will start with an example initial condition of $u(x,0) = 1 - \cos(x)$. In Fig. B.1, the solution becomes multivalued with time. The top panel shows snapshots of the wave at various times with the wave steepening with time. The bottom panel shows the characteristics for the system. In this panel, you can see that by $t = 1$, the characteristics have intersected and the solution has become multivalued. This solution is not physical for a hyperbolic system.
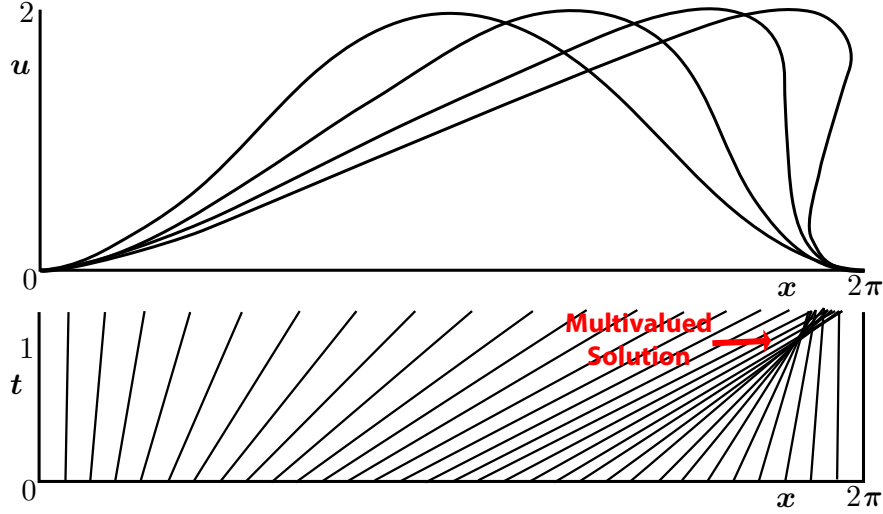
FIG. B.1. The reproduction of Figs. 3.4 and 3.5 from von Dommelen (2011) show the steepening of a wave resulting in a multivalued solution at times greater than $t = 1$. The top panel shows snapshots of u as it evolves with time. The bottom panel shows the characteristics for the system. In the lower panel, a red arrow indicates where the solution has become multivalued.

To avoid a multivalued solution, viscosity, ε, can be added to the right-hand side of (B.3) forming

$$\frac{\partial u}{\partial t} + u\frac{\partial u}{\partial x} = \varepsilon\frac{\partial^2 u}{\partial x^2}. \tag{B.3}$$

Beginning with the same initial condition as the inviscid case, we can see from the top panel of Fig. B.2 that the solution no longer overturns and becomes multivalued. Instead, a jump discontinuity has developed from our smooth initial condition. In the bottom panel, the characteristic curves no longer intersect after $t = 1$. In this case, the characteristics merge and are not unique in this region. This pattern in the characteristic curves denotes a shock in u.

As noted by Whitham (1974) and LeVeque (2002), over a prolonged period, the structure and information from the initial condition are lost in the shock. This means that shocks in non-linear systems represent an irreversible phenomena due to the characteristics disappearing at the shock.
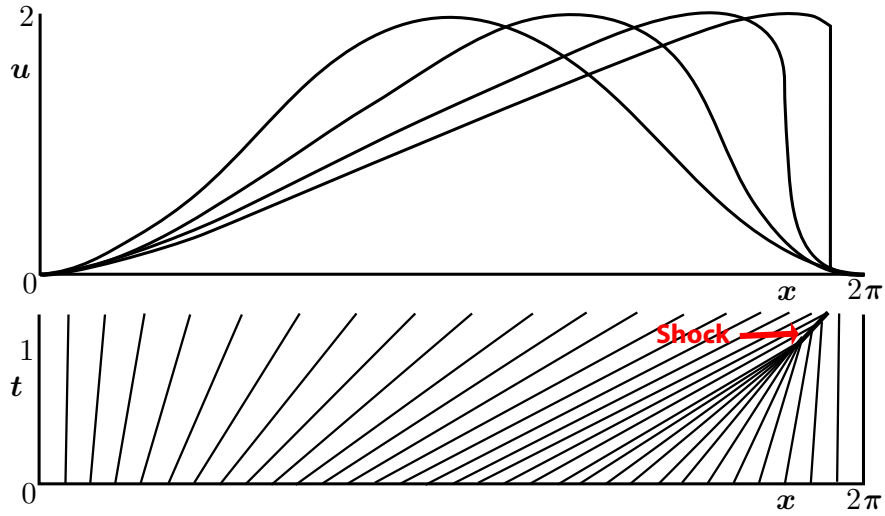
FIG. B.2. The reproduction of Figs. 3.6 and 3.7 from von Dommelen (2011) show shock formation by $t = 1$ from a smooth initial condition. The top panel shows snapshots of u as it evolves with time. The bottom panel shows the characteristics for the system. In the lower panel, a red arrow indicates where the shock has developed.